**Eur. Phys. J. C manuscript No.**
(will be inserted by the editor)

# Production, characterization and operation of $^{76}$Ge enriched BEGe detectors in GERDA

**M. Agostini[14], M. Allardt[3], E. Andreotti[5,17], A.M. Bakalyarov[12], M. Balata[1], I. Barabanov[10], N. Barros[3], L. Baudis[18], C. Bauer[6], N. Becerici-Schmidt[13], E. Bellotti[7,8], S. Belogurov[11,10], S.T. Belyaev[12], G. Benato[18], A. Bettini[15,16], L. Bezrukov[10], T. Bode[14], D. Borowicz[2,4], V. Brudanin[4], R. Brugnera[15,16], D. Budjáš[14], A. Caldwell[13], C. Cattadori[8], A. Chernogorov[11], V. D'Andrea[1,a], E.V. Demidova[11], A. Domula[3], V. Egorov[4], R. Falkenstein[17], K. Freund[17], N. Frodyma[2], A. Gangapshev[10,6], A. Garfagnini[15,16], C. Gotti[8,b], P. Grabmayr[17], V. Gurentsov[10], K. Gusev[12,4,14], W. Hampel[6], A. Hegai[17], M. Heisel[6], S. Hemmer[15,16], G. Heusser[6], W. Hofmann[6], M. Hult[5], L.V. Inzhechik[10,c], L. Ioannucci[1], J. Janicskó Csáthy[14], J. Jochum[17], M. Junker[1], V. Kazalov[10], T. Kihm[6], I.V. Kirpichnikov[11], A. Kirsch[6], A. Klimenko[6,4,d], K.T. Knöpfle[6], O. Kochetov[4], V.N. Kornoukhov[11,10], V.V. Kuzminov[10], M. Laubenstein[1], A. Lazzaro[14], V.I. Lebedev[12], B. Lehnert[3], H.Y. Liao[13], M. Lindner[6], I. Lippi[16], A. Lubashevskiy[6,4], B. Lubsandorzhiev[10], G. Lutter[5], C. Macolino[1,a], B. Majorovits[13], W. Maneschg[6], M. Misiaszek[2], I. Nemchenok[4], S. Nisi[1], C. O'Shaughnessy[13,e], D. Palioselitis[13], L. Pandola[1,f], K. Pelczar[2], G. Pessina[7,8], A. Pullia[9], S. Riboldi[9], N. Rumyantseva[4], C. Sada[15,16], M. Salathe[6], C. Schmitt[17], J. Schreiner[6], O. Schulz[13], B. Schwingenheuer[6], S. Schönert[14], E. Shevchik[4], M. Shirchenko[12,4], H. Simgen[6], A. Smolnikov[6], L. Stanco[16], H. Strecker[6], C.A. Ur[16], L. Vanhoefer[13], A.A. Vasenko[11], K. von Sturm[15,16], V. Wagner[6], M. Walter[18], A. Wegmann[6], T. Wester[3], H. Wilsenach[3], M. Wojcik[2], E. Yanovich[10], P. Zavarise[1], I. Zhitnikov[4], S.V. Zhukov[12], D. Zinatulina[4], K. Zuber[3], G. Zuzel[2]**

[1] INFN Laboratori Nazionali del Gran Sasso, LNGS, Assergi, Italy
[2]Institute of Physics, Jagiellonian University, Cracow, Poland
[3]Institut für Kern- und Teilchenphysik, Technische Universität Dresden, Dresden, Germany
[4]Joint Institute for Nuclear Research, Dubna, Russia
[5]Institute for Reference Materials and Measurements, Geel, Belgium
[6]Max Planck Institut für Kernphysik, Heidelberg, Germany
[7]Dipartimento di Fisica, Università Milano Bicocca, Milano, Italy
[8]INFN Milano Bicocca, Milano, Italy
[9]Dipartimento di Fisica, Università degli Studi di Milano e INFN Milano, Milano, Italy
[10]Institute for Nuclear Research of the Russian Academy of Sciences, Moscow, Russia
[11]Institute for Theoretical and Experimental Physics, Moscow, Russia
[12]National Research Centre "Kurchatov Institute", Moscow, Russia
[13]Max-Planck-Institut für Physik, München, Germany
[14]Physik Department and Excellence Cluster Universe, Technische Universität München, München, Germany
[15]Dipartimento di Fisica e Astronomia dell'Università di Padova, Padova, Italy
[16]INFN Padova, Padova, Italy
[17]Physikalisches Institut, Eberhard Karls Universität Tübingen, Tübingen, Germany
[18]Physik Institut der Universität Zürich, Zürich, Switzerland

Received: date / Accepted: date

arXiv:1410.0853v1 [physics.ins-det] 3 Oct 2014

[a] *also at:* INFN Gran Sasso Science Institute, L'Aquila, Italy
[b] *also at:* Università di Firenze, Firenze, Italy
[c] *also at:* Moscow Inst. of Physics and Technology, Russia
[d] *also at:* Int. Univ. for Nature, Society and Man "Dubna", Dubna, Russia
[e] *Present Address:* U. North Carolina, Chapel Hill, USA

**Abstract** The GERmanium Detector Array (GERDA) at the Gran Sasso Underground Laboratory (LNGS) searches for the neutrinoless double beta decay ($0\nu\beta\beta$) of $^{76}$Ge. Germanium detectors made of material with an enriched $^{76}$Ge fraction act simultaneously as sources and detectors for this decay.

During Phase I of the experiment mainly refurbished semi-coaxial Ge detectors from former experiments were used. For the upcoming Phase II, 30 new $^{76}$Ge enriched detectors of broad energy germanium (BEGe)-type were produced. A subgroup of these detectors has already been deployed in GERDA during Phase I.

The present paper reviews the complete production chain of these BEGe detectors including isotopic enrichment, purification, crystal growth and diode production. The efforts in optimizing the mass yield and in minimizing the exposure of the $^{76}$Ge enriched germanium to cosmic radiation during processing are described. Furthermore, characterization measurements in vacuum cryostats of the first subgroup of seven BEGe detectors and their long-term behavior in liquid argon are discussed. The detector performance fulfills the requirements needed for the physics goals of GERDA Phase II.

**Keywords** germanium detectors · enriched $^{76}$Ge · neutrinoless double beta decay ·

**PACS** 29.40.Wk solid-state detectors · 23.40.-s $\beta$ decay; double $\beta$ decay; electron and muon capture · 27.50.+e mass $59 \leq A \leq 89$ ·

## 1 Introduction

The GERmanium Detector Array (GERDA) [1,2,3,4] is an experiment at the Laboratori Nazionali del Gran Sasso (LNGS) of INFN searching for the neutrinoless double beta ($0\nu\beta\beta$) decay of $^{76}$Ge. It uses high-purity germanium (HPGe) detectors that are enriched in $^{76}$Ge to (86-88)% as sources and as detection media. The detectors are mounted in low-mass holders and are embedded in liquid argon (LAr), which serves as a cryogenic coolant and absorber against external radiation. A tank filled with ultrapure water provides a 3 m thick water buffer around the cryostat and serves as an additional absorber and as a Cherenkov muon veto.

The experimental signature of $0\nu\beta\beta$ decay is a peak in the spectrum of the summed energies of the two electrons released in the nuclear process. The peak should arise at the $Q_{\beta\beta}$ value which in the case of $^{76}$Ge is at (2039.061±0.007) keV [5]. The expected number of signal events $\lambda_S$ is given by:

$$\lambda_S = \frac{\ln 2 \cdot t}{T^{0\nu}_{1/2}} \cdot \frac{N_A \cdot M}{m_{enr}} \cdot f_{76} \cdot f_{av} \cdot \varepsilon_{fep} \cdot \varepsilon_{psd} \qquad (1)$$

where $T^{0\nu}_{1/2}$ is the half life of the $0\nu\beta\beta$ decay, $t$ the live time of the measurement, $N_A$ the Avogadro constant, $m_{enr}$ the molar mass of the enriched material and $M$ the total detector mass. The parameters $f_{av}$ and $f_{76}$ correspond to the fraction of the detector volume that is active, and to the $^{76}$Ge isotopic fraction, respectively. The efficiency $\varepsilon_{fep}$ corresponds to the fraction of events that deposit their entire energy at $Q_{\beta\beta}$ inside the active volume without bremsstrahlung loss. Finally, $\varepsilon_{psd}$ represents the efficiency of the signal acceptance by pulse shape discrimination (PSD).

The number of background events $\lambda_B$ in the region of interest (ROI) around $Q_{\beta\beta}$ scales in a first approximation with the detector mass. It can be expressed as follows:

$$\lambda_B = M \cdot t \cdot BI \cdot \Delta E \quad . \qquad (2)$$

$BI$ is the background index for the ROI around $Q_{\beta\beta}$ in units of cts/(keV·kg·yr) and $\Delta E$ is the width of the search window which depends on the energy resolution at $Q_{\beta\beta}$.

If the experiment can be carried out background-free, the sensitivity on the half life scales with $M \cdot t$. In case of a sizable background contribution ($\lambda_B >> 1$), its statistical fluctuation can be assumed to be Gaussian and the sensitivity would scale approximately with $\sqrt{(M \cdot t)/(\Delta E \cdot BI)}$.

GERDA has been conceived to proceed in different phases in order to fulfill a quasi background-free condition in each of them. A sensitivity scaling almost linearly with the exposure of the experiment is aimed for.

In Phase I semi-coaxial Ge detectors from the Heidelberg-Moscow (HDM) [6] experiment and the International Germanium Experiment (IGEX) [7] were deployed after their refurbishment. A background level of an order of magnitude lower than in those former experiments was achieved within Phase I [2].

For GERDA Phase II another factor of ten in background reduction is envisioned. This can only be achieved with an optimized experimental design with particular care for the detectors. After several years of R&D, a customized version of the broad energy germanium (BEGe) detector [8] from Canberra with a thick entrance window has been selected. The key to the superior rejection of background of these detectors lies in the simple and powerful analysis of the digitized waveform of the detector signals. In addition, external background events are either fully absorbed in LAr or can be

[f] *Present Address:* Laboratori Nazionali del Sud, INFN, Catania, Italy
[g] *Correspondence*, email: gerda-eb@mpi-hd.mpg.de

**Table 1** Measured isotopic composition and calculated density of the $^{76}$Ge enriched germanium for GERDA Phase II BEGe detectors. The reported measurements were performed via electron ionization and thermal ionization mass spectrometry (EI-MS, TI-MS) at ECP in Zelenogorsk, Russia, via neutron activation (k0NAAA) at IRMM in Geel, Belgium, and by means of inductively coupled plasma mass spectrometry (ICP-MS) at LNGS in Assergi, Italy. For comparison, the isotopic composition and density of natural germanium and of the GERDA $^{76}$Ge depleted BEGe detectors were added.

| technique | Ref. | $^{70}$Ge | $^{72}$Ge | $^{73}$Ge | $^{74}$Ge | $^{76}$Ge | calculated density [g/cm$^3$] |
|---|---|---|---|---|---|---|---|
| EI-MS, TI-MS | ⋆) | 0.0002(1) | 0.0007(2) | 0.0016(1) | 0.1234(33) | 0.8742(36) | 5.540(5) |
| k0NAAA | [10] | 0.001(1) | 0.001(1) | 0.001(1) | 0.130(2) | 0.867(11) | 5.539(11) |
| ICP-MS | ⋆) | 0.0014(1) | 0.0003(5) | 0.0011(10) | 0.1065(141) | 0.8921(141) | 5.550(20) |
| **average** | | 0.001(1) | 0.001(1) | 0.001(1) | 0.120(12) | 0.877(13) | 5.540(18) |
| $^{nat}$Ge | [11] | 0.204(2) | 0.273(3) | 0.078(1) | 0.367(2) | 0.078(1) | 5.323(4) |
| $^{dep}$Ge BEGe | [12] | 0.223(8) | 0.300(4) | 0.083(2) | 0.388(6) | 0.006(2) | 5.303(11) |

⋆) measured by GERDA and/or ECP

largely rejected on an event-by-event basis by detecting scintillation light produced via interactions in LAr [9].

This paper documents the entire production process from the enrichment (section 2.1), the purification (section 2.2), the crystal growth (section 2.3) to the diode fabrication (section 2.4). The precautions applied during the BEGe detector production in order to reduce cosmogenic-induced radioisotopes are described in section 3.

In total, 30 BEGe detectors were produced from newly acquired enriched material with a $^{76}$Ge fraction of about 88%. The detectors were produced in two batches. The first one comprises seven detectors which were named GD32(A-D) and GD35(A-C). After their fabrication and characterization in vacuum cryostats (section 4) five of them were deployed in GERDA during the data acquisition period of Phase I. Their performance in LAr is discussed in section 5.

The performance of all 30 BEGe detectors operated in vacuum cryostats including an intercomparison and Monte Carlo (MC) studies will be presented in an upcoming publication.

## 2 Production of BEGe detectors for GERDA Phase II

GERDA is a $0\nu\beta\beta$ experiment aiming for a quasi background-free ROI. Therefore, highest resolution of the detectors and radiopurity of the entire setup are of paramount importance. Within the germanium detector types, the BEGe family combines advantageously high resolution and pulse shape discrimination possibilities (see section 4.1). The costs for enrichment of germanium in $^{76}$Ge from its natural abundance of 7.8% to about 88% are compensated for by those for the reduced number of detectors needed inclusive associated electronics. For full depletion of BEGe detectors of height of a few cm, adequate impurity levels of $\lesssim 10^{11}$ are needed to keep reverse bias voltages below 4 kV. This requires a proper purification before germanium crystals can be grown and converted into operational diodes.

### 2.1 Enrichment of $^{76}$Ge

The enrichment in $^{76}$Ge for GERDA Phase II detectors was performed at the Svetlana Department of the Joint Stock Company "Production Association Electrochemical Plant" (ECP) in Zelenogorsk, Russia [13]. Since it is possible to bind Ge in gaseous $GeF_4$ compounds which possess a relatively low vapor pressure at room temperature, the gas centrifuge technique can be applied. The overall procedure is the following:

1. $^{nat}$Ge fluorination: $^{nat}Ge \rightarrow {}^{nat}GeF_4$,
2. centrifugation process: $^{nat}GeF_4 \rightarrow {}^{enr}GeF_4$,
3. hydrolysis within balloons: $^{enr}GeF_4 \rightarrow {}^{enr}GeO_2$,
4. drying and calcination of $^{enr}GeO_2$.

Herein, $^{nat}$Ge corresponds to natural germanium; $^{enr}$Ge stands for $^{76}$Ge enriched germanium, which in the following will also be referred to as 'enriched'. The gas centrifuge processing at ECP involves a large number of centrifuges in series and parallel formations. A photo of one cascade of the gas centrifuge assembly is shown in Fig. 1.

The annual productivity of the Svetlana Department facility is about (80-100) kg of germanium at ∼88% enrichment in $^{76}$Ge. The production of the enriched germanium for the GERDA Phase II BEGe detectors started at the end of February 2005 and finished at the beginning of September 2005. In total, 53.4 kg of $GeO_2$ powder was produced, which corresponds to 37.5 kg of germanium enriched in $^{76}$Ge [14]. After enrichment several subsamples were measured for their isotopic abundances with different techniques. A summary of the re-

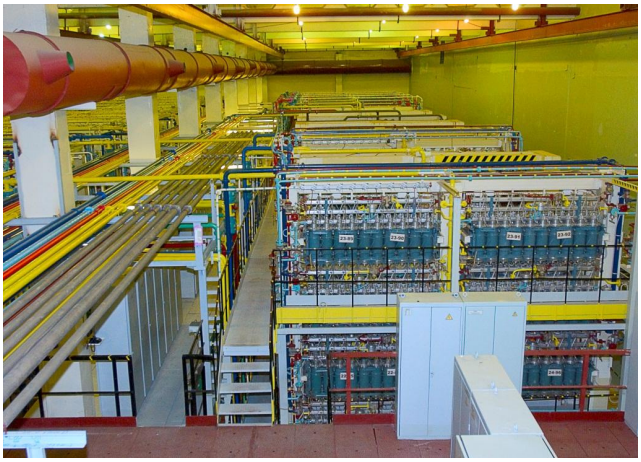

**Fig. 1** Photo of a small part of the gas centrifuge system at Svetlana department of ECP. Photo courtesy of ECP.

**Fig. 2** Final inventory after the zone-refinement of the enriched germanium used for the production of the GERDA Phase II detectors.

sults is given in Table 1. The table also includes the expected density of the final Ge crystals resulting from the isotopic compositions under the assumption of a pure face-centered cubic lattice. The density of enriched germanium remnants after crystal growth was measured by GERDA and resulted in an average value of (5.552 $\pm$0.003(stat.) $\pm$0.007(syst.)) g·cm$^{-3}$ at room temperature. This result is in very good agreement with expectations.

In addition to the enriched material, ECP provided 49.2 kg of $GeO_2$ depleted in $^{76}$Ge ($^{dep}$Ge; short form: 'depleted'). Its isotopic composition and calculated density are reported in Table 1. The depleted germanium was a by-product of the enrichment process and thus underwent the same chemical processing. For that reason it was purchased for testing the following purification via zone-refinement. Moreover, 34 kg of additional depleted material was purchased to test the full detector production chain including crystal growth and diode production and to develop characterization procedures. For further details see Ref. [12].

### 2.2 Reduction and purification of germanium

The ECP plant typically delivers $^{76}GeO_2$ powder of technical grade quality which corresponds to 99.8% purity level [13]. The quality depends on the purity of the initial samples of $^{nat}$Ge and $^{nat}GeF_4$, as well as on the purity during the chemical transformation of $^{enr}GeF_4$ to $^{enr}GeO_2$. For the construction of germanium diodes, however, germanium of electronic grade; i.e., 99.9999% purity (6N), has to be available before the start of crystal growth.

A first step in increasing the purity of the germanium was accomplished directly by ECP: improvements of clean conditions at work places, use of de-ionized water for hydrolysis etc. led to a 99.99% purity level (4N). This was certified by three different Russian laboratories: the Central Laboratory of ECP, the Analytic Certification Testing Center of the Institute of Microelectronics Technology & High Purity Materials [15], and the Certification Center of Giredmet [16].

For the transportation from Russia to Central Europe, the produced portions of enriched and depleted $GeO_2$ were filled into plastic bags of about 1 kg each. Before the start of the purification process of the $^{enr}GeO_2$, the material was stored in the HADES underground laboratory in Mol, Belgium, from April 2006 until March 2010.

For further purification, the company PPM Pure Metals GmbH [17] in Langelsheim, Germany, was selected. The overall procedure at PPM was the following:

1. $GeO_2$ reduction: the $GeO_2$ powder was reduced in $H_2$ atmosphere to metallic Ge. The resulting metal ingots were cleaned and etched.
2. The Ge metal ingots underwent zone-refinement (ZR). The zone-refined bars were etched before they were packed in plastic bags (see Fig. 2) and delivered for the next production steps.

The achievable purification level, the mass yield and the potential change in the isotopic composition were first tested with $^{dep}GeO_2$. After reduction and during ZR, measurements on extracted germanium subsamples were performed by means of inductively coupled plasma mass spectrometry (ICP-MS), spark source mass spectrometry (SS-MS) and resistivity measurements. 6N purity electronic grade germanium has an intrinsic resistivity of about 50 $\Omega$·cm. The low resistivity tails (<50 $\Omega$·cm) of the ingots were cut off and returned into the ZR furnace for 1-2 additional zone refining steps. The last remaining tail is typically too

**Fig. 3** Examples of a cylindrical (GD61B, left) and a conical (GD91A, right) crystal slice that were used for the production of GERDA Phase II BEGe detectors.

small to be reprocessed. The main conclusions from the experiences [12] with the $^{dep}GeO_2$ were:

1. The purity of the Ge metal after reduction is the same as for the initial $^{dep}GeO_2$. There was no sign that impurities were introduced.
2. No isotopic change was observed at the level of the measurement accuracy of ±0.01%.
3. The mass of the tail amounted to <1 kg which translates in this case to a mass yield of >90% for 6N material.

The following purification of the $^{enr}GeO_2$ in spring 2010 went smoothly. The purity of the $^{enr}GeO_2$ material was the same as for the $^{dep}GeO_2$. An overall mass yield of 6N germanium of 94.5% was obtained. Combined with the residual low resistivity tail, 97.7% of the original 37.5 kg of enriched germanium was finally available.

### 2.3 Crystal growth

For further zone refinement and crystal growth the 35.5 kg of 6N purified enriched germanium was sent to Canberra Industries Inc. [18], Oak Ridge (TN), USA.

The enriched germanium was further zone-refined to 11N material. Then crystal ingots with net carrier concentrations corresponding to 12N purity and with specified dimensions and crystal dislocation densities [19] were grown.

The crystal ingots were produced and delivered in two batches. The first two crystal ingots were grown in autumn 2011. Out of these seven crystal slices were cut according to an optimized production scheme which was developed by GERDA and Canberra during the depleted BEGe production [12]. After diode conversion (see section 2.4) and testing of the reliability of these first prototypes in spring 2012, seven more ingots were grown. In total, 23 additional crystal slices were obtained. Optimizing the mass yield was the main goal when selecting the actual cut; however, in general GERDA and Canberra aimed for specifications amongst them a diameter of 75 mm with a tolerance of ±5 mm, and a height of 30 mm with a tolerance of $^{+10}_{-5}$ mm. All but three crystal slices met these specifications. In two cases the diameters were 68.9 and 66.4 mm, and in one other case the height was 23.3 mm. The average diameter and height of all crystal slices was 73.3 and 29.7 mm, respectively, with ranges of about ±3 mm.

In optimizing the crystal slicing, conical tails and seed ends of ingots were also considered. As a result, 21 crystal slices are cylindrical, whereas nine are conical. Examples of a cylindrical and a conical crystal slice are depicted in Fig. 3. The combined mass of all crystal slices amounts to 20.8 kg. Approximately 8.8 kg of the loss was attributed to seed-end and tail-end crystal parts and crystal remainders, whereas 5.5 kg of kerf; i.e., a mixture of germanium shavings, water and lubricant, was collected in the process of grinding and lapping. All materials will be prepared for recycling, i.e. a further cycle of chemical purification and zone refinement before a new crystal growth.

All crystal slices for detector production and the crystal remainders were shipped back to Belgium and stored in the HADES underground laboratory (see section 3.2) until the beginning of diode conversion.

### 2.4 Diode production

The conversion of the germanium crystal slices into operational BEGe detectors was performed at Canberra Semiconductors N.V. [20], Olen, Belgium, since detailed

procedures had been developed in collaboration before. The functionality and properties of BEGe detectors will be discussed in sections 4.1 and 4.2.

Three diodes were usually produced per week. In the case of 29 diodes 13 g of the original crystal mass was lost on average due to the groove fabrication. In the case of detector GD76B, however, a larger crystal fraction of about 370 g (groove included) had to be removed to cure a micro-rupture situated a few mm under the surface.

Prior to the delivery of the detectors, Canberra tested the diodes for their basic parameters such as energy resolution, depletion voltage and leakage current as a function of the applied high voltage. The following requirements had to be met:

1. energy resolution: $< 2.3$ keV full width at half maximum (FWHM) of the 1333 keV $^{60}$Co $\gamma$-line,
2. operational (stable) voltage: $\leq 4$ kV,
3. leakage current: $< 50$ pA at depletion voltage.

Canberra was able to convert 29 out of 30 crystal slices into working detectors fulfilling all three criteria. The energy resolution for all 30 detectors is illustrated as a function of the detector mass in Fig. 4. The mean value of the energy resolution is (1.74±0.07) keV at 1333 keV. More details about the energy resolution, depletion voltage, active volume and other spectroscopic properties of a detector subset will be presented in section 4.3.

One crystal slice (GD02D) turned out to have a non satisfactory impurity distribution. This detector does not reach full depletion and the corresponding voltage plateau; therefore it has a deteriorated charge collection efficiency in some parts of the crystal. Nonetheless, this detector will be deployed in GERDA Phase II; its full or partial inclusion into the analysis can be decided later.

The production of GERDA Phase II BEGe detectors was optimized to achieve the highest possible mass transfer from the original enriched germanium to the final detector configuration. Out of 53.4 kg of $GeO_2$, containing 37.5 kg of elemental enriched germanium, 30 detectors with a total mass of 20.0 kg were fabricated. This corresponds to a mass yield of 53.3%. As shown in Table 2 the largest loss of germanium material occurred by cutting the crystal ingots and while grinding and lapping the crystal slices. The remainder are planned to be reprocessed.

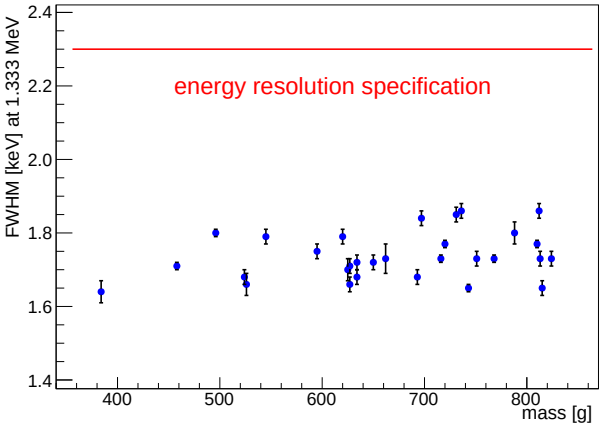


**Fig. 4** Energy resolution of all 30 GERDA Phase II BEGe detectors as a function of their masses. The energy resolutions are expressed as full widths at half maximum of the $^{60}$Co peak at 1333 keV. The error bars shown include only the uncertainties from the fit of the peaks. These were fitted with a step-like background and a Gaussian peak function.

## 3 Cosmic-ray activation of GERDA Phase II germanium

### 3.1 Cosmogenic production of radioisotopes in germanium

At sea level, secondary cosmic-rays consisting of fast nucleons (98%) as well as muons and muon-induced secondary neutrons (2%) produce long-lived radionuclides in materials via spallation reactions [21,22]. The subsequent decays of these radioisotopes generated inside the materials represent a serious source of background in rare-event physics experiments.

In germanium long-lived radioisotopes such as $^{68}$Ge ($T_{1/2}$=270.8 d) and $^{60}$Co ($T_{1/2}$=5.27 yr) are of main concern. The estimation of their production rate depends on the isotopic composition of the germanium, but also on varying neutron and proton fluxes at given locations and given times [22]. Even though the proton flux at sea level is only about 3% of the neutron flux, its contribution to the radioisotope production is about 10% due to the more efficient stopping of protons by ionizing interactions. The interpolated cross sections and semi-empirical models add further uncertainties. In literature the activation rates at sea level for

**Table 2** Mass yield from enriched germanium to the final 30 BEGe detectors for GERDA Phase II. The mass transfer fractions are given relative to the original enriched $GeO_2$ material (3rd column) and to the purified metallic Ge used for crystal growth (4th column).

| germanium operation | mass [kg] | rel. fraction [%] | [%] |
|---|---|---|---|
| Ge in $GeO_2$ after enrichment | 37.5 | 100.0 | – |
| purified Ge for crystal growth | 35.5 | 94.1 | 100.0 |
| cut crystal slices | 25.2 | 67.2 | 71.0 |
| grinded and lapped crystal slices | 20.8 | 55.5 | 58.6 |
| operational detectors | 20.0 | 53.3 | 56.3 |

**Table 3** Activation rates in nuclei/(d·kg) of cosmogenic-induced radionuclides $^{68}$Ge and $^{60}$Co in Ge isotopes, in natural and in enriched germanium according to Ref. [24]. In the case of the Ge isotopes the statistical standard deviations are in the range of (0.5-11)%.

| Ge isotope/ isotopic composition | neutron-induced $^{68}$Ge | neutron-induced $^{60}$Co | proton-induced $^{68}$Ge | proton-induced $^{60}$Co |
|---|---|---|---|---|
| $^{70}$Ge | 264.22 | 1.56 | 17.17 | 0.17 |
| $^{72}$Ge | 50.56 | 2.6 | 4.78 | 0.29 |
| $^{73}$Ge | 25.44 | 2.8 | 2.54 | 0.34 |
| $^{74}$Ge | 13.05 | 2.97 | 1.48 | 0.38 |
| $^{76}$Ge | 3.68 | 2.85 | 0.54 | 0.46 |
| $^{nat}$Ge | 74.84 | 2.56 | 5.60 | 0.32 |
| $^{enr}$Ge | 5.13 | 2.86 | 0.68 | 0.45 |

the two most prominent radioisotopes $^{68}$Ge and $^{60}$Co in enriched germanium (assuming 86% $^{76}$Ge and 14% $^{74}$Ge) vary between (1.0-13) and (1.6-6.7) nuclei/(d·kg), respectively [23]. For the following considerations the production rates of $^{68}$Ge and $^{60}$Co reported in Table 3 are applied. They are based on the excitation functions generated with the SHIELD code [24]. Regarding the enriched germanium used in GERDA Phase II detectors, the respective $^{68}$Ge and $^{60}$Co activation rates at sea level are 5.8 and 3.3 nuclei/(d·kg). In these cases, saturation at sea level is reached at ∼2300 $^{68}$Ge and ∼9200 $^{60}$Co nuclei/kg.

The contribution of the decays of $^{68}$Ge and $^{60}$Co radioisotopes to the *BI* of GERDA Phase II detectors has been evaluated by means of MC simulations [3,25]. The exponentially decreasing background was averaged over the first three years of data collection in GERDA Phase II. The $^{68}$Ge and $^{60}$Co radioisotopes would contribute with $3.7\times10^{-3}$ and $8.4\times10^{-4}$ cts/(keV·kg·yr) to the *BI* around $Q_{\beta\beta}$ assuming 100 nuclei per kg detector mass for each of them. A PSD analysis (see section 4.3.3) by itself can further reduce this to $1.8\times10^{-4}$ and $8.4\times10^{-6}$ cts/(keV·kg·yr), respectively.

Without pulse shape analysis, however, ∼30 nuclei of $^{68}$Ge or ∼120 nuclei of $^{60}$Co per kg germanium would already account for the allowed background budget of $10^{-3}$ cts/(keV·kg·yr). Such concentrations in $^{68}$Ge and $^{60}$Co are already reached after ∼5 and ∼36 d of exposure of unshielded enriched germanium at sea level, respectively. This makes it mandatory to restrict the overall exposure to sea level cosmic radiation during detector processing to a few days. As a consequence, large efforts were made to minimize activation of the enriched germanium during the entire production and characterization chain of the GERDA Phase II BEGe detectors.

### 3.2 Actions to minimize activation of germanium

*Active removal of $^{68}$Ge and $^{60}$Co during germanium processing:* During the enrichment process the centrifugation of the germanium fluoride compounds separates light nuclides from the heavy fraction containing $^{76}$Ge. The lighter stable Ge isotopes, which have larger activation cross sections for $^{68}$Ge compared to heavier Ge isotopes, are suppressed. As a consequence, the $^{70}$Ge abundance was reduced by more than three orders of magnitude from 20.54 to 0.01% (see Table 1). Since $^{70}$Ge has a ∼70 times higher $^{68}$Ge production rate at sea level than $^{76}$Ge, a reduction of $^{70}$Ge during the enrichment of $^{76}$Ge considerably reduces the $^{68}$Ge activation rate. In total, the production rate of $^{68}$Ge in enriched germanium is decreased by a factor of ∼14 compared to natural germanium. The activation rate for $^{60}$Co in enriched germanium is similar to the one of natural germanium, as there is no significant dependence of the activation rate on the mass number of the germanium nucleus.

During chemical purification, zone refinement, and during growth of germanium monocrystals impurities of U and Th as well as $^{60}$Co are efficiently removed. Note, however, that during these refinement steps $^{68}$Ge cannot be separated.

*Optimization of germanium processing steps:* A significant exposure to cosmic radiation occurs during unshielded processing at the manufacturer sites. GERDA cooperated with all the manufacturers to optimize their standard procedures in terms of speeding up their processing steps. In case of the enrichment process, a notable improvement was achieved. After the successful centrifugation and separation of light from heavy isotopes, the production of new $^{68}$Ge and $^{60}$Co nuclides starts right away as portions of gaseous $GeF_4$ flow from the last stages of the cascade to the receiving balloons. According to ECP standard technology, the collection of a GERDA-sized batch of $GeF_4$ into balloons, the chemical conversion of this compound to germanium dioxide and the drying and calcination process would last 40 d on average. Following an upgrade of the production plant the average time of production of the GERDA portion of enriched germanium above ground was reduced to 74 h (3.1 d).

*Storage on-site:* As stated before, the germanium material was processed at different sites throughout above ground. At these processing sites the germanium was stored in nearby shallow or deep underground (UG) locations whenever it was not needed for processing. Table 4 summarizes the processing steps applied during

**Table 4** Underground locations close to the manufacturer sites that were selected for the production of GERDA Phase II BEGe detectors. The shielding power is expressed in terms of meters of water equivalent (m w.e.).

| processing step | location | UG site | shield [m w.e.] | distance [km] |
|---|---|---|---|---|
| enrichment | ECP, Zelenogorsk, RU | concrete bunker | 5 | <1 |
| purification to 6N | Langelsheim, GER | Rammelsberg mine | 80 | 10 |
| crystal growth | Oak Ridge, TN, USA | Cherokee cavern | 50 | 7 |
| diode production | Olen, BE | HADES | 500 | 30 |
| detector characterization | Mol, BE | HADES | 500 | 30 |
| operation in GERDA | Assergi, IT | GERDA at LNGS | 3500 | – |

the production of the GERDA Phase II BEGe detectors, the sites where these steps were performed, and the respective UG sites. Moreover, the approximate shielding powers in terms of meters of water-equivalent (m w.e.) of the UG sites and their distances to the manufacturers' sites are also given. The processing was planned in close cooperation between the manufacturers and the on-site GERDA collaborators that were responsible for almost daily transportation of the material between the UG and processing sites.

*Transport:* The transport of the enriched germanium from one processing site to another was arranged in containers by truck and ship. Transport by aircraft was excluded *a priori* since the cosmic-ray exposure in the higher atmosphere is larger by orders of magnitude compared to sea level [26]. Since the transportation times were substantial, which would lead to an unacceptable *BI* contribution in GERDA Phase II, a shielded transport container was designed and built.

For the transport of $GeO_2$ powder from Zelenogorsk to Munich in February and March 2006 a protective cylindric steel container was used [24]. Its dimensions are 140 cm(D)×126.5 cm(H) with a total weight of 14.5 t. Inside the container a cavity of 54 cm(D)×40 cm(H) can accommodate all the germanium. The expected reduction factor of germanium activation due to nuclear as well as muon components from cosmic rays was in the range of 10 for $^{68}$Ge and 15 for $^{60}$Co [24]. To demonstrate the possibility of transportation, a conveyance from Zelenogorsk to Munich was accomplished in 2005. The journey lasted 20 d. Taking the effect of shielding into account this corresponds to ∼2 d of exposure at sea level.

For further transports (including the return shipment from Europe to USA for crystal growth) the container was upgraded. As shown in Fig. 5 the empty cavities between the container roof and the steel shield were filled with jerry cans containing water with 30 g salt per liter. The overall thickness of the water shield is 70 cm increasing the tare weight of the shielded container to 26 t. According to simulations [27], both the $^{68}$Ge and $^{60}$Co production rates are further reduced by about a factor of two.

### 3.3 Tracking the exposure history and achieved activation levels

Starting from the enrichment phase, all periods between each processing and transportation step above ground were documented in detail in a database. Assuming a given production rate at sea level [24] and taking the transport container [24,27] the expected number of $^{68}$Ge and $^{60}$Co nuclei in each individual germanium piece can be estimated for any given time.

Figure 6 depicts the history of the estimated number of $^{68}$Ge and $^{60}$Co nuclei produced in one enriched BEGe detector (GD32A). The activation history starting with the enrichment is shown up to September 1, 2014. The individual processing steps and transport periods can be clearly identified by the increase of the number of nuclei during the unshielded times. Periods in which the germanium was shielded deep under-

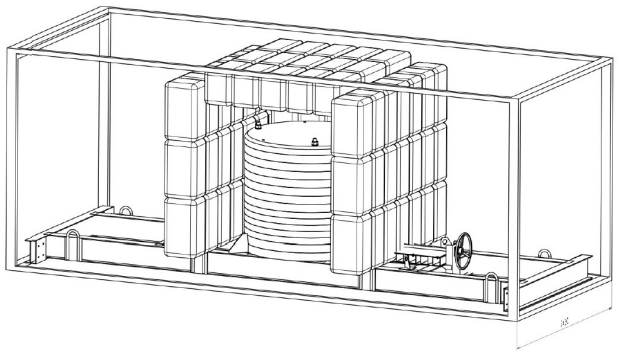

**Fig. 5** Sketch of the shielded container used for the transport of the GERDA germanium material enriched in $^{76}$Ge. The shield has an inner iron container. This is surrounded by jerry cans filled with salt water and has a cavity to accommodate the germanium material. For visibility of the steel shield the front wall of the water jerry cans has been omitted.

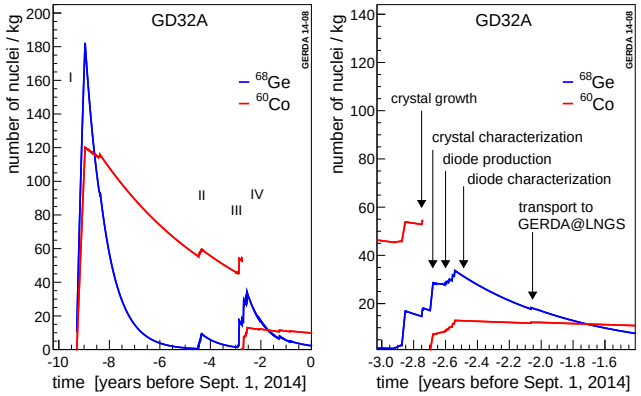


**Fig. 6** Left: Full history of the estimated number of cosmogenic-induced $^{68}$Ge and $^{60}$Co atoms in $^{enr}$Ge used for the manufacturing of detector GD32A. Major activation occurred during enrichment (I), purification (II), crystal growth (III) and diode conversion (IV). $^{60}$Co was removed completely at the time of crystal growth. Right: Zoom of the exposure history of detector GD32A during its crystal growth and diode conversion.

ground become visible from the exponential decay of the shorter-lived $^{68}$Ge. The exposure histories of the other enriched BEGe detectors are similar to that of GD32A.

Table 5 summarizes the estimated amount of $^{68}$Ge and $^{60}$Co, respectively, by September 1, 2014, for the subset of detectors delivered first. On average, ∼5 $^{68}$Ge and ∼21 $^{60}$Co atoms/kg are expected. According to background studies by GERDA the decays of these radionuclides $^{68}$Ge and $^{60}$Co over a period of three years of non interrupted data collection will lead in both cases to a background rate of $1.8\times10^{-4}$ cts/(keV·kg·yr) at $Q_{\beta\beta}$ [3]. Taking advantage of the background rejection via pulse shape analysis (see section 4.2) the $BI$ contribution from the two radionuclides can be lowered to $9.1\times10^{-6}$ cts/(keV·kg·yr) and $1.8\times10^{-6}$ cts/(keV·kg·yr), respectively [25]. As a consequence, the background contribution from $^{68}$Ge and $^{60}$Co decays should be at least 50 times lower than the total $BI$ envisioned for GERDA Phase II, even if the production rates at sea level used in the current calculation were underestimated by factor of two.

**Table 5** Number of $^{68}$Ge and $^{60}$Co nuclei in the seven enriched BEGe detectors as of September 1, 2014, according to their exposure histories and the production rates in Ref. [24]. Due to the wide range of predicted production rates the reported numbers are quoted without uncertainties.

| detector | mass | $^{68}$Ge | | $^{60}$Co | |
|---|---|---|---|---|---|
| | [kg] | # | #/kg | # | #/kg |
| GD32A | 0.459 | 2.3 | 5.0 | 9.8 | 21.4 |
| GD35B | 0.717 | 4.1 | 5.8 | 18.6 | 26.0 |
| GD32C | 0.743 | 3.5 | 4.8 | 15.9 | 21.4 |
| GD32B | 0.723 | 3.6 | 4.9 | 15.3 | 21.1 |
| GD32D | 0.768 | 3.4 | 4.4 | 16.2 | 21.1 |
| GD35C | 0.812 | 3.1 | 3.9 | 13.6 | 16.8 |
| GD35A | 0.635 | 3.9 | 6.1 | 14.3 | 22.5 |
| Total | 4.857 | 23.9 | 4.9 | 103.7 | 21.4 |

## 4 Detector characterization in vacuum

After confirmation of proper functionality, stable operation and detector parameters by the manufacturer, the GERDA collaboration performed cross-checks ('acceptance tests') of the manufacturer specifications and characterization tests. The goal was to characterize detector properties that cannot be easily accessed by the manufacturer or by GERDA after integration into the experiment.

Before discussing the measurements by GERDA and the results obtained for the first seven enriched BEGe detectors in section 4.3, some basic concepts of BEGe-type detectors are introduced in sections 4.1 and 4.2.

### 4.1 Design of BEGe detectors

GERDA has chosen a modified thick window Broad Energy Germanium (BEGe) detector manufactured by Canberra as the detector type for Phase II. Compared to the semi-coaxial detectors used in GERDA Phase I, the BEGe detector design shows smaller dimensions and thus smaller mass. Due to a different layout of the electrodes (see Fig. 7) the electric field profile in BEGe detectors differs strongly from the one in semi-coaxial detectors.

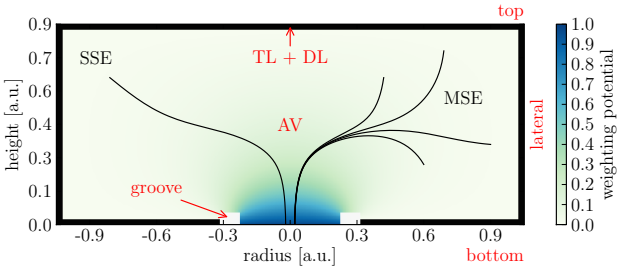


**Fig. 7** Generic view of a BEGe diode. The p+ read-out electrode (center, bottom) is separated from the n+ electrode by a groove covered by an insulating passivation layer. The n+ electrode consisting of an inactive dead (DL) and transition (TL) layer with reduced charge collection surrounds the active volume (AV). The dimensionless weighting potential is color-coded and strongest close to the p+ electrode. Examples of a single-site event (SSE) and of a multi-site event (MSE) are illustrated by means of the hole trajectories of the individual energy depositions.

The selected BEGe detectors are made of p-type germanium; they comprise a 'wrap around' n+ electrode known as 'lithium dead layer', a p+ electrode acting as electron blocking contact, and an intercontact insulating surface. The first two items are achieved by lithium diffusion and boron implantation. For the third item a small annular concentric groove between the p+ and n+ electrodes is produced and covered by an insulating silicon monoxide layer which is known as 'passivation layer'. This layer helps to keep steady-state currents (so-called 'leakage currents') stable over time. The currents are induced on the detector surface and in the bulk by some finite conductivity in the reverse direction and should be kept at a few tens of pA.

In p-type BEGe detectors the dimensionless 'weighting potential' $\Phi$ shown in Fig. 7 peaks strongly close to the central p+ electrode. Ionization will create electrons and holes which drift due to the applied potential and the field created by the space charge of the depleted diode. The time dependent induced current $I(t)$ on the p+ electrode is given by the Ramo-Shockley theorem [28] as:

$$I(t) = q \cdot \mathbf{v}(\mathbf{r}(t)) \cdot \nabla\Phi(\mathbf{r}(t)) \tag{3}$$

where $q$ stands for the drifting charge and $\mathbf{v}(\mathbf{r}(t))$ for the drift velocity at position $\mathbf{r}(t)$. Holes drift to the p+ electrode along the region around the central axis, irrespective of the starting point ('funnel' effect); $I(t)$ peaks at the end of the drift where $\nabla\Phi$ is largest. Hence, the maximum $A$ of $I(t)$ is directly proportional to the deposited energy $E$. Electrons drift through volumes with low $\nabla\Phi$ and hardly contribute to $A$. That means that $A/E$ is constant for all single-site events (SSE) except for ionizations in a small volume close to the p+ electrode [8,12,29]. In contrast, for multi-site events (MSE) the drift times of holes from several simultaneous energy depositions are in general different and hence $A/E$ of the summed signal is reduced. For ionizations in the n+ transition layer (like from surface $\beta$-events) the diffusion time is comparable to the drift time and hence $A/E$ is also reduced. For p+ surface events electrons drift through the volume with largest $\nabla\Phi$, and hence $A/E$ is larger than for SSE due to the increased displacement current. The latter is also the case for events close to the groove.

The layout imposes tighter constraints on the impurity and defect concentrations in the starting crystal material that are more demanding to achieve. These requirements arise due to the non-coaxial electrode arrangement in BEGe detectors and the resulting electric field profile in order to achieve complete charge collection within the detector volume.

### 4.2 General properties of BEGe detectors

*Depletion voltage:* The depletion voltage of a Ge detector is defined as the reverse bias voltage that electrically fully depletes the diode of free charge carriers. It strongly depends on the net impurity concentration and its gradient, on the detector dimensions and on the read-out electrode sizes. The best performance in terms of energy resolution is achieved at full depletion but it is necessary to keep the leakage currents small. The depletion voltage is usually determined via an irradiation of the detector with a $\gamma$-ray calibration source and a stepwise increase of the voltage up to the value recommended by the manufacturer. During this high voltage (HV) scan, detector operational parameters such as the energy resolution $\Delta E$, the peak position and the peak integral of prominent $\gamma$-lines are monitored. As soon as the detector is electrically fully depleted, these parameters reach almost constant plateaus. The measured curves are fitted. Then, the depletion voltages are defined as those fit points, at which 99% of the optimal $\Delta E$ and maximum peak count rate as well as 99.9% of the highest peak position is obtained. Note that a $\sim$1 ‰ drift of the peak position corresponds to a $\sim$1 keV shift in energy, a $\sim$1% reduced peak integral to a $\sim$1% reduced active volume, and a $\sim$1% lower energy resolution to a $\sim$0.02 keV broader $\gamma$ peak – all at $\sim$1 MeV $\gamma$s detected by a BEGe detector.

*Active volume:* The p-type BEGe detectors (Fig. 7) have an internal active volume (AV) in which the charge collection efficiency (CCE) is maximal ($\epsilon = 1$). Gamma-rays fully absorbed in this volume contribute to the full-energy peaks (FEP). The AV is surrounded by a transition layer (TL) with reduced CCE ($0 < \epsilon < 1$) and a low electric field [30]. Charges released in this region diffuse into the AV only in part. Finally, the TL is covered by a thin conductive lithium-doped layer in which the CCE is entirely suppressed ($\epsilon = 0$) (see section 4.1) and is therefore called dead layer (DL). This notation is more detailed because of the specific dependence of GERDA on the $0\nu\beta\beta$ signal and possible partial energy losses. Previously, in standard $\gamma$-ray spectroscopy DL and TL were lumped together as a single totally inactive 'dead layer'.

A precise knowledge of the detector-specific active volume (AV) and its uncertainty is of great importance for GERDA. There are two possibilities to determine it. Firstly, high energy calibration sources can be used to irradiate directly the AV. Secondly, low energy probes are used to measure the full-charge collection depth (FCCD); i.e., the sum of TL and DL thicknesses. In this case, the AV fraction $f_{av}$ is deduced via a subtraction of

the FCCD volume from the detector volume which was calculated from the measured geometrical dimensions. Complementary measurements are needed in order to reduce systematic uncertainties. A difficulty in scanning is present since detectors are housed in cryostats with thick end caps. This was overcome via a surface scan with low energy $\gamma$-ray sources able to penetrate the cryostat endcaps.

*Pulse shapes:* Efficient background suppression is of paramount importance for GERDA. $0\nu\beta\beta$ events in germanium are characterized by the absorption of two emitted $\beta$-particles within a small volume of few mm$^3$ which is interpreted as a SSE. On the contrary, $\gamma$-rays of similar energy can undergo multiple Compton scattering leading to MSE. Based on these pulse shape differences background events can be identified and suppressed.

In order to study the pulse shape discrimination (PSD) power, high energetic $\gamma$-ray calibration sources are often used. Further, fine-grained surface scans with collimated low energy $\gamma$-ray probes help in understanding local differences in the pulse shape response and deduce detector intrinsic properties such as the crystal lattice and electron and hole mobilities in germanium.

## 4.3 Tests in vacuum cryostats

All 30 GERDA Phase II BEGe detectors were delivered in a Canberra dip stick vacuum cryostat of type 7500SL with a 4" endcap diameter [31]. Characterization tests were performed in the HADES underground research laboratory in Mol, Belgium, at 30 km distance from the diode manufacturer. Inside HADES an area of $\sim$14 m$^2$ was equipped with several static measurement tables and automatized movable scanning setups, 33 radioactive sources, and two types of data acquisition systems: Multi-Channel Analyzers (MCA) and 100 MHz Struck Flash Analog Digital Converters (FADC). The signals were read out with a charge sensitive preamplifier provided by Canberra (model 2002CSL) and – in case of the FADC systems – digitized. Then, the energy $E$ and the maximum of the current pulse $A$ were reconstructed by digital signal processing using a semi-Gaussian shaping. This offline analysis was performed with the software tool GELATIO [32] following the procedure described in Ref. [33]. Data storage systems and a network for remote control and data transfer were installed. This infrastructure, called HEROICA, had a screening capacity of two detectors per week in case only standard measurements were performed. A more detailed description of the screening facility can be found in Ref. [34].

Most of the tests applied to the new enriched BEGe detectors are based on campaigns and protocols of natural and depleted BEGe detectors [12] which served as prototypes to verify the production chain and the detector performance compared to former detector designs. In addition, several non-standard tests were applied on particular detectors. In the case of the active volume (AV) determination, for instance, many systematic effects were investigated. These included a remeasurement of the diode masses and dimensions, a crosscheck of the diode position inside the cryostat endcap, dead time uncertainty estimations, germanium density measurements, and intercomparisons of source activities and of MC code versions.

### *4.3.1 Depletion voltage and energy resolution*

The depletion voltage of the first seven enriched BEGe detectors was measured by using pointlike $^{60}$Co sources and performing high voltage (HV) scans in steps of (50-100) V typically from 500 V up to the voltage $V_r^C$ of several kV which was recommended by Canberra. At each intermediate voltage point the energy spectrum was measured and three parameters were monitored: the peak position (PP), the peak integral (PI) and the energy resolution $\Delta E$ of the two $^{60}$Co $\gamma$-lines. $\Delta E$ is expressed in terms of FWHM and was calculated via a fit function consisting of a Gaussian distribution for the peaks and a step-like function describing the background and Compton continua.

The HV scan curves of the detectors GD32A and GD35B are depicted exemplarily in Fig. 8 and 9. The three curves of a single detector converge to an almost constant value at approximately the same voltage. Within this study the depletion voltages $V_{d,\Delta E}$, $V_{d,PP}$, $V_{d,PI}$ were deduced, at which the single parameters reach an almost constant value as described in section 4.2. Table 6 summarizes the results obtained for the seven enriched BEGe detectors. In particular, the following observations are made:

($i$) The measured reference voltages typically fulfill the relation $V_{d,PI} \lesssim V_{d,PP} \lesssim V_{d,\Delta E}$. The values $V_{d,PI}$, $V_{d,\Delta E}$ and $V_{d,PP}$ are compatible for both 1173 keV and 1333 keV $\gamma$-lines. The detectors are usually operated at the voltage $V_r^C$ recommended by the manufacturer, who measures typically only the peak position $V_{d,PP}^C$ vs. voltage. The value of $V_r^C$ is usually 500 V above the measured $V_{d,PP}^C$ value. Canberra's $V_{d,PP}^C$ values are slightly higher than the voltage region defined by GERDA in which the PP is above 99.9% of its maximum value. This guarantees that the three detector parameters will always be in an optimum region for operation.

**Table 6** Voltage parameters and energy resolutions of the first seven enriched BEGe detectors for GERDA. Measurements performed by the manufacturer Canberra and by GERDA are marked by 'C' and 'G', respectively. All other abbreviations are explained in the text. The manufacturer results were provided without an uncertainty quotation. The GERDA voltage values have uncertainties of around ±200 V. Due to the systematic uncertainties the values for the energy resolution are rounded to the significant digits.

| detector | voltage | | energy resolution | | |
|---|---|---|---|---|---|
| | $V_r^C$; $V_{d,PP}^C$ [kV] | $V_{d,PI}^G$;$V_{d,PP}^G$;$V_{d,\Delta E}^G$ [kV] | $\Delta E^C$ [keV] at 1333 keV | $\Delta E^G$ [keV] at 1333 keV | $\Delta E^G$ [keV] at 2615 keV |
| GD32A | 3.0; 2.5 | 2.1; 2.4; 2.6 | 1.695 | 1.73 | 2.46 |
| GD32B | 4.0; 3.5 | 2.1; 2.7; 3.0 | 1.747 | 1.77 | 2.49 |
| GD32C | 4.0; 3.5 | 2.9; 3.2; 3.7 | 1.658 | 1.70 | 2.41 |
| GD32D | 4.0; 3.5 | 2.2; 2.7; 2.8 | 1.757 | 1.65 | 2.45 |
| GD35A | 4.0; 3.0 | 2.6; 2.6; 2.7 | 1.785 | 1.71 | 2.40 |
| GD35B | 4.0; 3.5 | 2.5; 2.9; 3.5 | 1.748 | 1.80 | 2.57 |
| GD35C | 3.5; 3.0 | 2.3; 3.0; 3.3 | 1.643 | 1.78 | 2.50 |

(*ii*) The reference energy resolution $\Delta E$ of the seven BEGe detectors was deduced from a measurement in which they were operated at the recommended voltage $V_r^C$.

The peaks were fitted with a Gaussian function and a step-like plus a constant background term. The uncertainties due to the fit are at the 10 eV level. The systematic uncertainty is estimated in this case to 0.03 keV. All detectors have a similar $\Delta E$. For the $\gamma$-lines from $^{60}$Co and $^{208}$Tl decays at 1333 and 2615 keV the averaged values are (1.73±0.05) and (2.47±0.05) keV, respectively. All the $\Delta E$ values are ∼30% better than those of the GERDA semi-coaxial detectors operated in vacuum cryostats (see Ref. [35]). In general, the GERDA $\Delta E$ values are in good agreement with the manufacturer's specifications.

(*iii*) The parameter dependencies of all detectors follow expectations from the known impurity densities and geometries of the detectors. For detectors GD35A and GD35B (Fig. 9) the curves of all three parameters were found to be very similar. The diode and read-out electrode geometries of the two detectors are comparable, and the impurity concentrations – as confirmed by the manufacturer – are similar. Moreover, both detectors exhibit the so-called 'bubble' [36] or 'pinch-off' effect [37]: In a voltage interval of a few tens of volts just below the depletion voltage, an island in the central region forms in which the total electric field becomes zero. Depending on their starting position almost all charge clouds drifting to the read-out electrode might cross this island and get affected. This gives rise to the observed broader energy resolution and a peak position instability, which leads in the above two cases to a discontinuity around (2.3-2.7) kV.

### *4.3.2 Active volume determination*

The active volume fractions $f_{av}$ of the seven enriched BEGe detectors were determined by an intercomparison of calibration data with simulated calibrations of the same experimental setup [38]. Calibration spectra were taken for two complementary types of $\gamma$-ray sources.

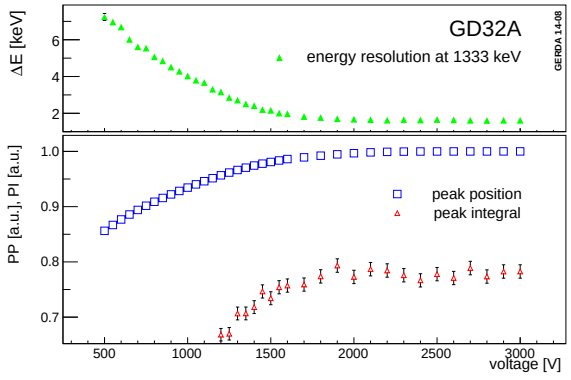


**Fig. 8** $^{60}$Co HV scan of detector GD32A: energy resolution $\Delta E$ (as FWHM at 1333 keV), peak position (PP) and peak integral (PI) as functions of the applied voltage.

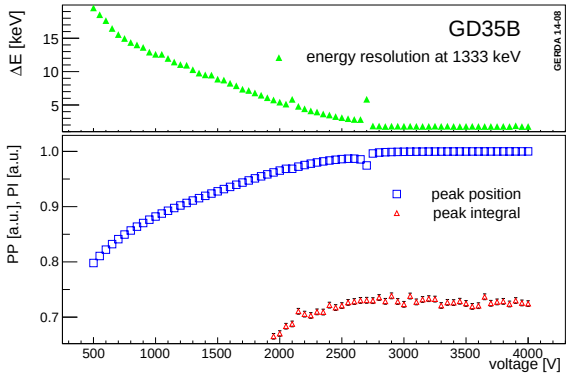


**Fig. 9** Same as in Fig. 8 for GD35B. A discontinuity around 2.7 kV is visible which originates from the so-called 'bubble/pinch-off' effect.

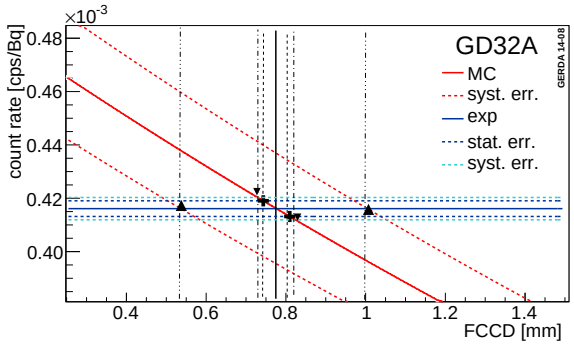


**Fig. 10** Extraction of the FCCD value of detector GD32A from a comparison of the measured vs. simulated absolute count rate of the 1173 keV $\gamma$-line of $^{60}$Co: MC simulated value as a function of FCCD (red), measured observable (blue), intersection (black).

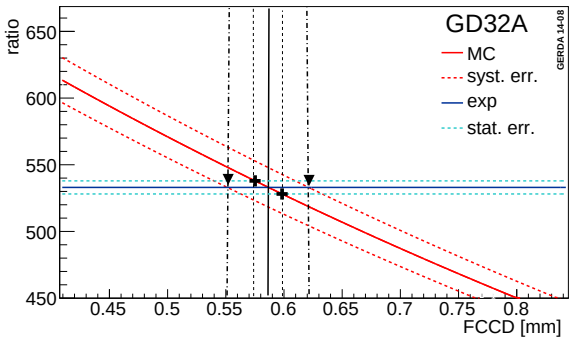


**Fig. 11** Extraction of the FCCD value of detector GD32A from a comparison of the measured vs. simulated ratio of two $\gamma$-line intensities for $^{241}$Am. Lines are color-coded as in Fig. 10.

Firstly, uncollimated low-energy $\gamma$-ray emitting $^{241}$Am sources were deployed 19.8 cm away from the cryostat endcap to probe the FCCD and thus the combined TL and DL thickness. The $f_{av}$ fractions are deduced indirectly by subtraction of the summed TL and DL volume from the overall detector volume. Secondly, higher energy $^{60}$Co sources with an activity of $\sim$(6-14) kBq were positioned at the same distance from the cryostat endcaps as in the case of the $^{241}$Am sources. $^{60}$Co sources with activities calibrated at a $\pm$1% level were used to probe directly the AV by irradiating the entire bulk of the detector diode.

MC simulations were performed in the MaGe [39] software framework based on Geant4 [40,41] version 9.4.p04. Simulations of both source measurement types were performed for all detectors. Afterwards the peak counts of a subset of $\gamma$-ray peaks in the experimental and MC simulated energy spectra were evaluated by both a fitting and a counting method. Then, two types of observables; i.e., either count rates or count rate ratios, were extracted and plotted as a function of the FCCD. As a working hypothesis an equal FCCD thickness on the top, lateral and bottom sides of the detector surface was assumed. In the case of $^{60}$Co, the MC peak count rates were plotted as a function of the FCCD. An example is given in Fig. 10. The intersection of the experimental result and the simulated curve gives the FCCD of the detector. This method depends strongly on the precise knowledge of the detector dimensions, source activity and distance of source to detector. In case of $^{241}$Am, the ratio of the count rates in the 60 keV peak and the summed count rates from the neighboring peaks at 99 and 103 keV in the measured spectrum were compared with the corresponding ratios of MC spectra for different FCCD values. An example is given in Fig. 11. By using the peak count ratio, uncertainties emerging from the source-to-detector distance and the source activity cancel out. The intersection of the measured ratio and the MC ratios as a function of the FCCD thickness defines the average upper surface FCCD thickness and in consequence the AV of the detector.

The determined $f_{av}$ values based on $^{241}$Am and the 1173 keV $^{60}$Co $\gamma$-line are reported in Table 7. In summary:

($i$) reported central values and uncertainty budgets are slightly improved compared to a previous evaluation used in Refs. [2,3].

($ii$) The manufacturer used an $^{241}$Am surface probe to estimate the FCCD thicknesses. Translating these results into $f_{av}$ fractions, they are in good agreement at a 1% level with the $^{241}$Am results of the current analysis.

($iii$) The $f_{av}$ central values deduced from the $^{60}$Co measurements are systematically lower than the ones obtained via the $^{241}$Am surface tests. For two detectors the difference is at the 1% level, in the other five cases it is between 2 and 3%. On average, the difference is 1.9%. 28 potential sources of systematic uncertainties were evaluated. The most prominent contributions are reported in Table 8. For each detector the total systematic uncertainty was divided into a detector correlated and non-correlated part. An example for the first category is the usage of the same calibration source for all detectors, which – in case of an offset – would cause an asymmetric shift in one direction for all $f_{av}$ mean values. As shown in Table 7, the correlated systematic uncertainty of the $^{60}$Co measurements can explain the observed shift.

**Table 7** Active volume fractions ($f_{av}$) of the first seven enriched BEGe detectors for GERDA. The systematic uncertainties are split in detector correlated and uncorrelated contributions. The 6th column presents $f_{av}{}^{\star}$ where the uncertainties are added in quadrature. For comparison, the manufacturer specifications, which were provided without uncertainty, are reported in the last column.

| detector | $\gamma$-peak/nuclide | $f_{av}\ ^{+stat+ucorr+corr}_{-stat-ucorr-corr}$ | $f_{av}{}^{\star}$ | Canberra |
|---|---|---|---|---|
| GD32A | 1173 keV | $0.8962^{+0.0006+0.0066+0.0250}_{-0.0006-0.0060-0.0237}$ | $0.896^{+0.026}_{-0.024}$ | |
| | $^{241}$Am | $0.9229^{+0.0015+0.0009+0.0043}_{-0.0015-0.0009-0.0041}$ | $0.923^{+0.005}_{-0.004}$ | 0.922 |
| GD32B | 1173 keV | $0.8887^{+0.0010+0.0062+0.0258}_{-0.0010-0.0056-0.0244}$ | $0.889^{+0.027}_{-0.025}$ | |
| | $^{241}$Am | $0.9059^{+0.0012+0.0013+0.0037}_{-0.0012-0.0013-0.0036}$ | $0.906^{+0.004}_{-0.004}$ | 0.899 |
| GD32C | 1173 keV | $0.9069^{+0.0030+0.0064+0.0262}_{-0.0030-0.0058-0.0248}$ | $0.907^{+0.027}_{-0.026}$ | |
| | $^{241}$Am | n/a | n/a | 0.923 |
| GD32D | 1173 keV | $0.9129^{+0.0039+0.0062+0.0262}_{-0.0039-0.0056-0.0247}$ | $0.913^{+0.027}_{-0.026}$ | |
| | $^{241}$Am | $0.9316^{+0.0030+0.0006+0.0038}_{-0.0030-0.0006-0.0037}$ | $0.932^{+0.005}_{-0.005}$ | 0.921 |
| GD35A | 1173 keV | $0.9262^{+0.0005+0.0063+0.0261}_{-0.0005-0.0057-0.0246}$ | $0.926^{+0.027}_{-0.025}$ | |
| | $^{241}$Am | $0.9369^{+0.0006+0.0012+0.0031}_{-0.0006-0.0012-0.0030}$ | $0.937^{+0.003}_{-0.003}$ | 0.927 |
| GD35B | 1173 keV | $0.9236^{+0.0013+0.0075+0.0264}_{-0.0013-0.0070-0.0249}$ | $0.924^{+0.027}_{-0.026}$ | |
| | $^{241}$Am | $0.9406^{+0.0054+0.0016+0.0038}_{-0.0056-0.0015-0.0036}$ | $0.941^{+0.007}_{-0.007}$ | 0.923 |
| GD35C | 1173 keV | $0.9036^{+0.0025+0.0079+0.0251}_{-0.0025-0.0073-0.0238}$ | $0.904^{+0.026}_{-0.025}$ | |
| | $^{241}$Am | $0.9288^{+0.0013+0.0010+0.0042}_{-0.0014-0.0010-0.0040}$ | $0.929^{+0.005}_{-0.004}$ | 0.926 |

*4.3.3 Background rejection via pulse shape analysis*

For the determination of the background rejection efficiency of the new BEGe detectors via pulse shape analysis, uncollimated $^{228}$Th calibration sources were deployed on the outer surface of the vacuum cryostat endcaps. The double escape peak (DEP) of the 2615 keV photons appears at 1593 keV. Most DEP events are like $0\nu\beta\beta$ decays – they are SSE unless bremsstrahlung leads to energy losses. Contrarily, the full energy peak (FEP), the single escape peak (SEP) and Compton continua events correspond mainly to MSE. The obtained $A/E$ vs. $E$ plot for detector GD32D is shown exemplarily in Fig. 12. Herein, the $A/E$ values of the events were computed after a 10 ns differentiation and threefold 50 ns integration of the charge signal.

As a standard, a low side $A/E$ cut was set, which keeps 90% of the events in the Compton-background subtracted DEP. Then the survival fractions of FEP,

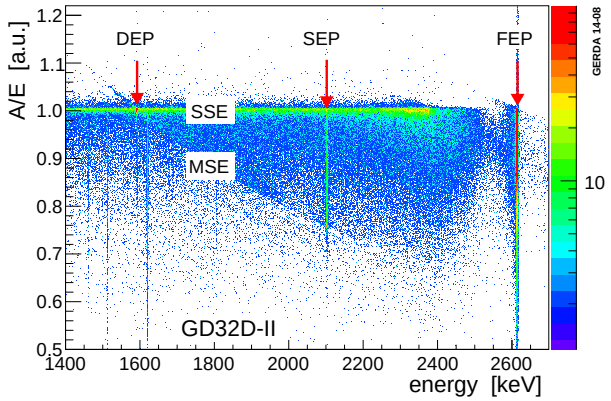


**Fig. 12** The $A/E$ ratio vs. energy $E$ from events of a $^{228}$Th calibration of detector GD32D-II.

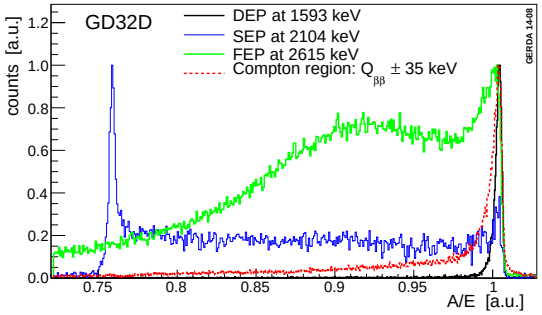


**Fig. 13** The $A/E$ distributions for selected energy intervals obtained from a $^{228}$Th calibration of detector GD32D: full energy peak (FEP), single escape peak (SEP) and double escape peak (DEP) events belonging to the 2615 keV $^{208}$Tl $\gamma$-line (Compton-subtracted). The $A/E$ distribution of Compton-scattered events in the 70 keV interval around $Q_{\beta\beta}$ is also shown.

**Table 8** Main systematic uncertainties considered in the determination of the $f_{av}$ fractions. All systematic contributions are given in % with respect to the count rate of $^{60}$Co or to the ratio for $^{241}$Am except for the dead time uncertainties (*) which are first translated into a live time uncertainty. This depends on the respective live time of the single measurement, which was typically >97%. In the case of $^{241}$Am, two sources with different uncertainties were used. Thus, both numbers are reported.

| category | systematics | uncert. [%] ($^{60}$Co) | uncert. [%] ($^{241}$Am) |
|---|---|---|---|
| MC physics processes | GEANT4 physics [42] | ±4 | ±2 |
| | $\gamma$-line intensity 1173 keV | ±0.03 | - |
| | $\gamma$-line intensity 1333 keV | ±0.0006 | - |
| | $\gamma$-line intensity $^{241}$Am | - | ±1.5 |
| $\gamma$-ray source | source activity | ±1 | 0 |
| | source material | ±0.01 | ±0/ ± 0.014 |
| | source geometry | ±0.02 | ±0.013/ ± 0.016 |
| detector and cryostat | detector dimension | ±2.5 | - |
| | dist. source to endcap | ±1.2 | - |
| | endcap geometry | ±0.15 | ±0.31 |
| | dist. detector to endcap | ±1.0 | - |
| | detector cup geometry | ±0.06 | ±0.03 |
| | detector cup material | ±0.03 | ±0.01 |
| dead time | MCA dead time (*) | ±10 | - |
| | FADC dead time (*) | ±5 | - |
| shaping time | shaping time | ±0.2 | - |

SEP and Compton events in the energy region between (1-2.6) MeV were studied (see Fig. 13). A high side $A/E$ cut is only needed to reject surface events occurring close to the p+ electrode.

$A/E$ distributions of DEP events must exhibit a narrow Gaussian peak in order to obtain a reasonable PSD efficiency. To satisfy the needs of the GERDA experiment a FWHM of $\lesssim$1% is required. However, a small tail component of MSE with lower $A/E$ from underlying bremsstrahlung background is allowed. SSE populating the peak can then be disentangled from the tail region. The PSD results are reported in Table 9.

It was found that: ($i$) A single $A/E$ peak was observed in GD32B, GD35B and in most of the prototype BEGe detectors. However, multiple-peak structures and/or an unusual broad peak were observed in five of the enriched BEGe detectors (GD32(A,C,D), GD35(A,C)). Fig. 14 shows one well-performing detector and two detectors with a deteriorated $A/E$ performance.

Setup-related artifacts were excluded by remeasuring the PSD behavior of the prototype depleted BEGe detector denoted with 2/B. This detector was previously measured in other laboratories and led to very similar results (compare Table 9 reported here with Table 4 in Ref. [12]). Malfunctioning electronic components inside the cryostat endcaps were excluded by reusing them for different BEGe detectors. No notable noise effects and time instabilities were identified. Correlations among the $A/E$ distribution shape and macroscopic properties such as impurity concentrations or gradients, operational voltages, crystal slice types and crystal shapes were not found. However, positive charged compounds can be deposited in the groove on the passivation layer between the p+ and n+ electrodes after diode production. This can deform the electric field configuration leading to distorted drift paths. This assumption has been substantiated by dedicated measurements with collimated $^{241}$Am and $^{228}$Th sources. Moreover, the grooves of the detectors GD32C and GD32D underwent chemical treatment by the manufacturer followed by heating. The first detector was affected by operational instabilities after reprocessing, but the second one clearly improved its PSD behavior.

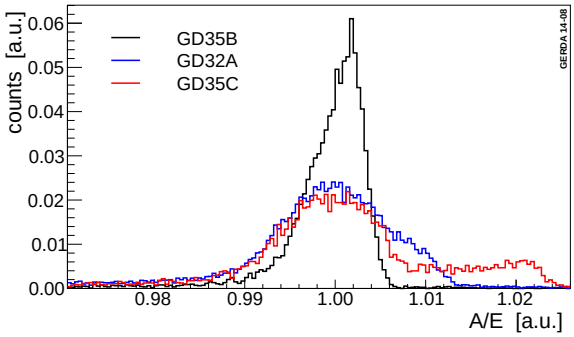


**Fig. 14** $A/E$ distributions of DEP events from $^{208}$Tl decays measured for three enriched BEGe detectors. For comparison the distributions were normalized. GD35B can be described by one single Gaussian with $\lesssim$1% resolution plus a tail on its left side. GD32A and GD35C have a resolution of $\gtrsim$1%. In addition, GD35C has a multiple structure.

**Table 9** Gamma-ray background survival fractions (in percentages) of the first seven enriched BEGe detectors operated in vacuum cryostats. For comparison, the performance of the prototype BEGe detector denoted with 2/B [12] is reported as well. In the case of the detector GD32D, the pulse shape performance was measured before (I) and after (II) a rework of the groove. The $A/E$ widths $b_{A/E}$ are by trend correlated with the obtained PSD efficiencies. For the DEP the uncertainty is statistical only, while for the others the total uncertainty is quoted. The relative uncertainty of the $b_{A/E}$ fit calculation is in the range of few percent.

| detector | DEP at 1593 keV | SEP at 2104 keV | FEP at 2615 keV | ROI (2004-2074) keV | $b_{A/E}$ [%] |
|---|---|---|---|---|---|
| 2/B | 90.0±0.9 | 4.7±0.5 | 7.0±0.4 | 31.0±1.0 | 0.6 |
| GD32A | 90.0±0.5 | 12.2±0.4 | 16.3±0.7 | 42.8±0.7 | 1.3 |
| GD32B | 90.0±0.9 | 5.3±0.5 | 8.8±0.5 | 33.0±0.8 | 0.8 |
| GD32C | 90.0±1.1 | 8.3±0.7 | 11.3±0.4 | 40.0±0.9 | 1.5 |
| GD32D-I | 90.0±1.1 | 14.7±1.2 | 22.1±1.6 | 47.0±1.3 | 1.5 |
| GD32D-II | 90.0±0.5 | 5.7±0.3 | 7.4±0.3 | 38.3±0.8 | 0.7 |
| GD35A | 90.0±1.0 | 7.8±0.5 | 13.1±0.6 | 39.5±0.7 | 2.4 |
| GD35B | 90.0±0.8 | 5.7±0.4 | 7.1±0.4 | 33.0±0.8 | 0.9 |
| GD35C | 90.0±0.7 | 10.0±0.8 | 15.1±0.9 | 40.3±1.2 | 2.8 |

The $A/E$ anomaly was further investigated with two enriched BEGe detectors without passivation layer and operated in liquid argon, as described in section 5.2.

(*ii*) The detectors GD32B and GD35B have PSD efficiencies similar to the prototype natural and depleted BEGe detectors [12]. As shown in Table 9 the survival fractions of MSE lying in the SEP and FEP are around (6-9)%, while Compton events in the region of interest (ROI) around $Q_{\beta\beta}$ survive at a ∼33% level. The uncertainties reported include statistical and systematic contributions. For all five other cases the PSD efficiency is deteriorated due to the $A/E$ anomaly. In the extreme case of GD32D, the survival probability for the $\gamma$-lines and intervals increases to (15-22)% and 47%, respectively.

### *4.3.4 Surface scans with $^{241}$Am sources*

Six out of the first seven GERDA Phase II BEGe detectors were scanned at several hundred position on the top and lateral site (nomenclature referring to Fig. 7) with a novel automatized setup consisting of a motorized mechanical arm. The arm is equipped with a collimated 5 MBq $^{241}$Am source. The diameter of the collimator hole is 1 mm. Further details are reported in Ref. [34].

The 60 keV $\gamma$-rays emitted by the $^{241}$Am source have a typical penetration depth of 1 mm in germanium. This leads to an energy deposition near the detector surface in form of a single charge cloud.

*FCCD homogeneity and diode position:* For this purpose, the count rates of the 60 keV $\gamma$-rays in single positions along linear axes were measured.

The observed count rate drops at the edges and allowed the comparison of the diode positions inside the cryostat endcaps with the callout in the technical drawings of the manufacturer. No misalignment was found within ±1 mm.

Along the bulk of the diodes most of the seven detectors showed a stable count rate. GD32C, for instance, has an almost constant count rate profile (see Fig. 15). A few detectors like GD35B, however, fluctuate up to ±30% translating into a ∼0.1 mm [43] FCCD difference. The count rate profile on the front side area of these detectors is characterized by higher count rates at the center and at the outermost borders. The origin of the observed fluctuation has not yet been understood.

*Spatial dependence of the pulse shape response:* The pulse shapes of events in a $\pm 4.5\,\sigma$ region around the 60 keV $\gamma$-peak were investigated for every scanned point. Especially the variation of the $A/E$ peak positions over the entire surface was studied. Detectors not affected by the $A/E$ anomaly; i.e., the detectors GD32B and GD35B were measured to have a rather good $A/E$ peak stability with variations of 1%. The other enriched BEGe detectors showed stronger deviations up to 4.5% going

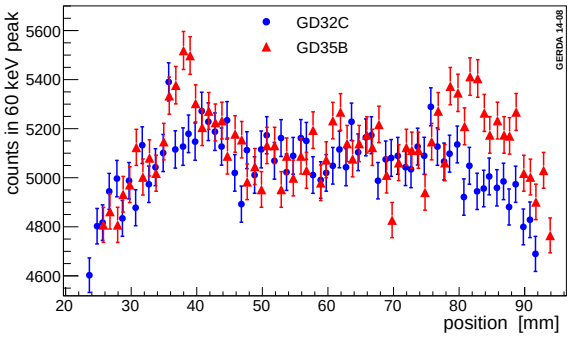


**Fig. 15** Count rate profile from a linear scan along the top side surface of the detectors GD32C and GD35B.

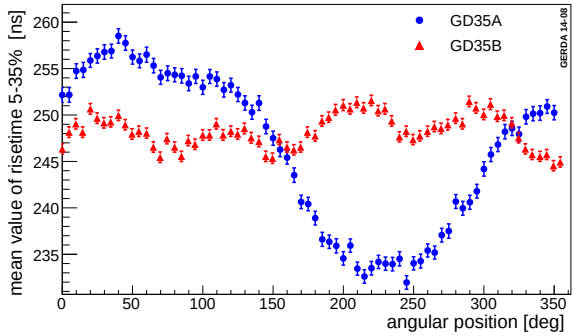


**Fig. 16** Mean value of the (5-35)% interval of the rise time slope of the pulses registered along a lateral side scan of GD35A and GD35B.

from the exterior towards the center. This observation is consistent with the working hypothesis that the origin of the $A/E$ anomaly is due to non homogeneously distributed charge carriers on the passivation layer (see section 4.3.3).

A similar behavior was observed for the mean (5-35)% rise time interval of the registered pulses, which represents the main drift path through the crystal from the interaction point to the p+ electrode. Detectors GD35B (see Fig. 16), GD32B and 2/B indicated a 90° oscillation due to the different drift mobilities for holes along the axes of the faced-centered cubic crystal lattice of germanium [44]. However, for the other enriched BEGe detectors such as GD35A (Fig. 16) the 90° oscillation was overwhelmed by a much larger 180° oscillation most likely caused by a one-sided concentration of charges in the groove.

## 5 Detector performance in liquid argon

Since the beginning, GERDA has foreseen the parallel usage of different Ge detector designs. The long-term stability and the pulse shape performance of BEGe detectors have been studied with prototype natural and depleted BEGe detectors for vacuum cryostat operation [12,8] and in LAr [45]. It was also desirable to confirm the low intrinsic background of the new detectors – in particular for possible surface $\alpha$-contamination potentially introduced during manufacture. For this check an ultra-low background environment, such as inside the GERDA set-up, was necessary. Therefore, the GERDA collaboration decided to operate five of the new enriched BEGe detectors already during Phase I of the experiment. This also allowed the study of their operational stability over a period of ∼320 d as well as their PSD *in situ*. The results are presented in section 5.1. The positive performance permitted to add 3 kg to the total mass in GERDA Phase I.

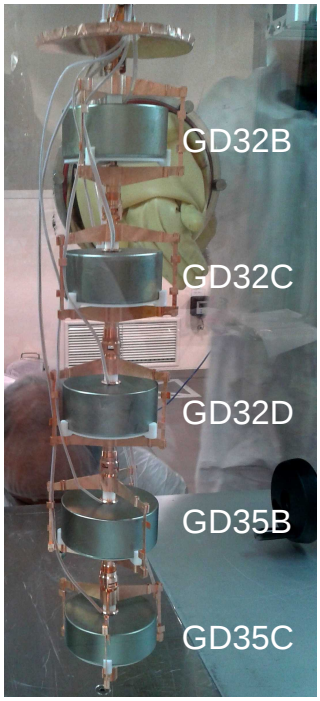


**Fig. 17** The string of five enriched BEGe detectors before deployment into GERDA (July 6, 2012).

The two remaining enriched BEGe detectors which were affected by the $A/E$ anomaly (section 4.3.3) under vacuum conditions were reworked in order to investigate possibilities to improve the PSD performance. For this purpose, the passivation layer of these detectors was removed. The results are discussed in section 5.2.

### 5.1 Operation of enriched BEGe detectors in GERDA Phase I

Detectors GD32B, GD32C, GD32D, GD35B and GD35C, were mounted into the GERDA cryostat without prior removal of the passivation layer surrounding the readout electrode. Their configuration is shown in Fig. 17 prior to their insertion into the GERDA cryostat. Data taking relevant for the Phase I analysis started on July 8, 2012, and stopped on May 21, 2013.

All five enriched BEGe detectors were operated at the same voltage of 3500 V. According to Table 6 this voltage is equal or even larger than the voltages recommended by the manufacturer. According to the GERDA characterization measurements in section 4.3.1 this voltage guarantees a maximum active volume and an optimal energy resolution for all detectors. Two detectors, GD35B and GD35C, were connected to the same HV line. Both detectors showed problems during oper-

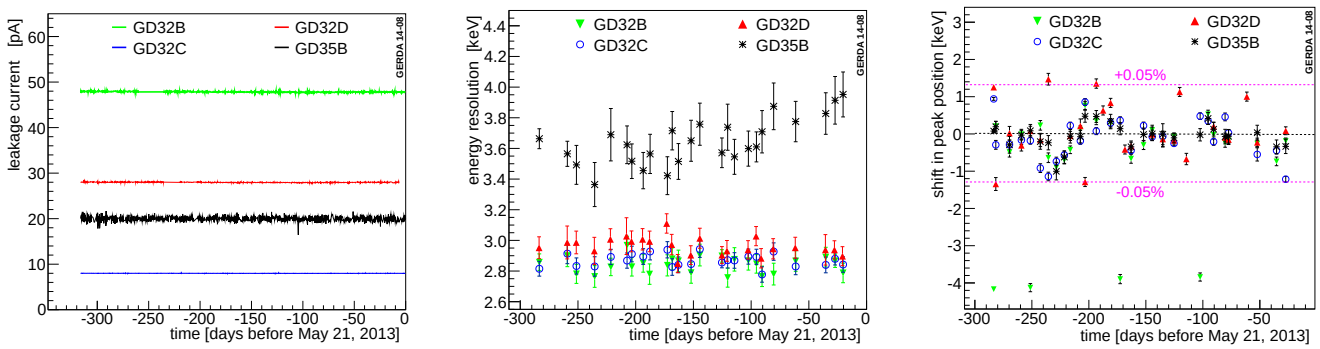


**Fig. 18** Operational stability of the four enriched BEGe detectors operated in LAr during GERDA Phase I: (left) Stability of leakage current $I_l$. The systematic uncertainty of ±4 pA is not shown. (middle) Time dependency of the energy resolution $\Delta E$ expressed in terms of FWHM of the $^{208}$Tl $\gamma$-line at 2615 keV. (right) Peak position variability of the $^{208}$Tl $\gamma$-line at 2615 keV.

ation: GD35B had microphonic noise leading to poor energy resolution, while detector GD35C experienced larger gain instabilities, which prevented useful data collection. This was possibly caused by an improper contact of the signal cable to the p+ electrode. Ignoring GD35C, the performance of the remaining four enriched BEGe detectors operated in GERDA Phase I is summarized in the following sections.

### *5.1.1 Stability of operational and spectroscopic parameters*

*Leakage current:* The leakage current $I_l$ was calculated from the voltage drop across the feedback resistor. It was monitored continuously for the four operational enriched BEGe detectors. Initially, $I_l$ was measured via the test point voltage of the detectors. During the long-term operation $I_l$ was extracted from the baseline of recorded events. As demonstrated in Fig. 18(left), $I_l$ of all detectors was acceptably low. The systematic uncertainty of ±4 pA is not shown. Additionally, $I_l$ was almost constant during the entire data collection time.

Almost weekly $^{228}$Th source calibration tests did not increase $I_l$. In the past, source measurements of several days duration conducted on prototype semi-coaxial detectors with a passivation layer led to a significant increase of $I_l$ [46]. For the passivated BEGe detectors in GERDA Phase I this was probably avoided by collecting enough statistics within only few hours.

*Energy resolution:* The energy resolution $\Delta E$ was determined by irradiating the four enriched BEGe detectors with $^{228}$Th sources in LAr, and by recording and processing data according to Ref. [1]. In total, 25 different calibration data sets for all detectors were available. The corresponding FWHM of the $^{208}$Tl $\gamma$-line at 2615 keV are depicted in Fig. 18(middle). All detectors had a good and stable $\Delta E$ over the entire period except GD35B. The averaged $\Delta E$ of the other three detectors ranged between 2.8 and 3.0 keV. The averaged $\Delta E$ of GD35B was at 3.6 keV, and there was an increase of 0.4 keV over this time period.

The $\Delta E$ values of the four enriched BEGe detectors operated in LAr were 30% worse than the values obtained for the same detectors operated in vacuum cryostats (see Table 6). This was expected, since the signal cable length in LAr between the read-out electrode and the first stage of the preamplifier, the field-effect transistor (FET), was longer by ∼30 cm. For GERDA Phase II, however, it is planned to place the FET closer to the read-out electrode. In addition, new offline energy reconstruction algorithms are under development that should further improve the energy resolution.

Finally, compared to the semi-coaxial Ge detectors operated in LAr with almost identical read-out electronics, the four BEGe detectors had a ∼30% better energy resolution [3].

*Peak position stability:* The energy scale stability of the four enriched BEGe detectors was measured by means of the $^{208}$Tl $\gamma$-peak at 2615 keV. As shown in Fig. 18(right) the peak position was relatively stable with deviations mostly within ±0.05%. Temporary instabilities in the energy scale of individual detectors were identified by analyzing the response to regularly injected charge pulses into the input of the amplifiers. Possibly, the signal and/or the HV contact was not stable. Data affected by the instabilities were excluded in the data analysis.

### *5.1.2 Pulse shape performance*

The pulse shape behavior of the four enriched BEGe detectors has already been discussed in the context of the pulse shape methods developed for GERDA Phase I data analysis [4]. It has been pointed out, that the mean

**Table 10** Gamma-ray background survival fraction (in percentages) of the four enriched BEGe detectors operated in LAr during GERDA Phase I. The relative uncertainty from the $A/E$ width $b_{A/E}$ fit calculation is in the range of few percent. For the DEP the uncertainty is statistical only, while for the others the total uncertainty is quoted. For a direct comparison of the FEP and SEP efficiencies with Table 9 one should consider a systematic contribution of 1% due to geometric effects from different detector-source configurations in LAr and vacuum.

| detector | DEP at 1593 keV | SEP at 2104 keV | FEP at 2615 keV | ROI (2004-2074) keV | $b_{A/E}$ [%] |
|---|---|---|---|---|---|
| GD32B | 90.0±0.9 | 11.4±0.7 | 15.1±1.0 | 44.3±1.0 | 1.5 |
| GD32C | 90.0±0.8 | 11.3±0.7 | 14.7±0.9 | 45.9±1.0 | 1.7 |
| GD32D | 90.0±1.1 | 10.2±0.7 | 14.2±0.9 | 45.2±1.2 | 1.6 |
| GD35B | 90.0±1.5 | 9.9±1.3 | 16.2±1.5 | 46.4±2.0 | 1.9 |

value $\mu_{A/E}$ of the Gaussian components describing the $A/E$ distributions was affected by two time variations. Firstly, an exponentially decreasing $\mu_{A/E}$ with a time period of ∼1 month was observed. The size of the total drift depended on the detector and varied from 1 to 5% (largest for GD32B). Secondly, a $\mu_{A/E}$ shift of 1% to higher values during $^{228}$Th source calibrations was observed. These instabilities were quantified and time-corrections were applied to the $A/E$ distributions of calibration and physics data. The origin of the dynamic processes is still under investigation. The observed dynamic $A/E$ drift might originate from charges present on the passivated groove, which neutralize or dissolve into the LAr over several months of operation.

The width $b_{A/E}$ of the $A/E$ distributions obtained from all calibration data turned out to be $\gtrsim$1.5% for the four BEGe detectors. This was sufficient for Phase I, however, a value $\leq$1% is aimed for Phase II. It was demonstrated that a $b_{A/E}$ of 1% can be achieved with BEGes in LAr (section 5.2).

In contrast to the Phase I analysis the acceptance of SSE-like DEP events at 1593 keV was fixed at 90%,

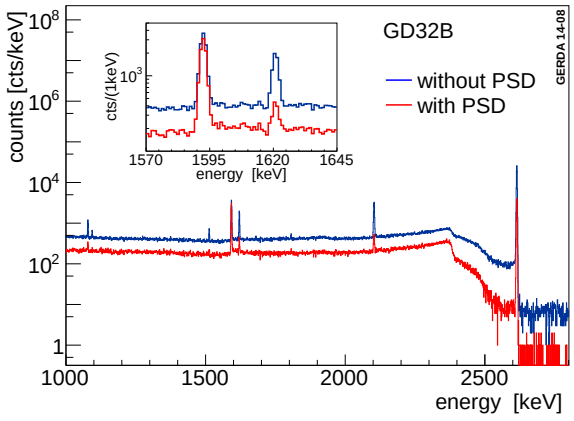


**Fig. 19** Application of the $A/E$ pulse shape method on GERDA $^{228}$Th calibration data collected with detector GD32B. SSE in the DEP at 1593 keV were retained at a fixed 90% level. The resulting survival fraction of other $\gamma$-lines and Compton regions are reported in Table 10.

in order to compare the performance of different detectors and set-ups, in particular with the vacuum tests. The resulting $\gamma$-ray background survival fractions are reported in Table 10. The energy spectrum before and after the application of the PSD cut is shown exemplarily for detector GD32B in Fig. 19. After Compton subtraction of the SEP and the FEP peaks, 89% and 85% of the $\gamma$-ray events are rejected in LAr. The values obtained from the same detectors operated in vacuum (see Table 9) are slightly higher, even considering an additional ∼1% uncertainty due to different source-detector distances in the two configurations. This was expected due to the less favorable electronics setup in GERDA Phase I compared to the operation in vacuum cryostats. Concerning the Compton-scattered $\gamma$-rays with energies around $Q_{\beta\beta}$ the events are rejected at ∼55% in LAr. Since the Compton continuum is dependent on the source distance and position, this value cannot be directly compared with the vacuum test results.

Finally, the PSD method was applied to the physics data of GERDA Phase I [2]. Herein, the $A/E$ acceptance cut on SSE-like events at $Q_{\beta\beta}$ was optimized differently than the one used for the $^{228}$Th calibration data collected in vacuum and in LAr. Firstly, events below and above the SSE band were cut. Secondly, the cut was relaxed to keep more SSE-like events. Thirdly, the cut was at a fixed normalized $A/E$ value instead of a fixed DEP acceptance; i.e. 0.965< $A/E$ <1.07. The final $A/E$ rejection efficiency of all background events in the ROI around $Q_{\beta\beta}$ was ∼82%, while (92±2)% of $0\nu\beta\beta$ events would survive the $A/E$ cut [2,4].

### *5.1.3 Background examination*

The background sources affecting the enriched BEGe detectors in GERDA Phase I have already been discussed in Ref. [3].

Gamma-rays induced by $^{214}$Bi and $^{228}$Th decays occuring in assembly materials close to the detectors were found to be the prevailing contaminants.

The predicted background induced by detector-intrinsic decays of the two dominant cosmogenic radioisotopes, $^{68}$Ge and $^{60}$Co, was presented in section 3.1. The spectral fit of the GERDA Phase I data revealed a good agreement with the expectations. The outcome reinforced the confidence that – with the knowledge of the exposure history of a detector to cosmic radiation – this background contribution can be reliably controlled.

The following paragraphs review some aspects of two other important contaminants which are not induced by gamma-rays and therefore their suppression relies on detector PSD instead of LAr scintillation anti-coincidence.

*Cosmogenic $^{42}$Ar in LAr:* The most critical external background for BEGe detectors in GERDA originates from $\beta^-$-emission of the $^{42}$Ar daughter nuclide $^{42}$K. The $\beta$-particles with energies up to 3525 keV have a total stopping power of up to 1.5 MeV·cm$^2$/g in natural germanium [47] and depending on distance are able to penetrate the n+ FCCD. According to Ref. [3], $^{42}$K $\beta$-events are expected to contribute at a ∼55% level to the total $BI$ of $(4.2\pm0.7)\times10^{-2}$ cts/(keV·kg·yr) of the four BEGe detectors in GERDA Phase I [4]. Thus, the $^{42}$Ar concentration should be either reduced or the induced background signals suppressed by PSD techniques.

Since the $^{42}$K $\beta$-surface events have typically long rise times it is possible to suppress them efficiently via PSD (see also Fig. 12 in Ref. [4]). The $A/E$ method led to a $^{42}$K survival fraction of few per cent, as expected from experimental investigations in Ref. [48]. The total $BI$ of the BEGe detectors operated in GERDA Phase I was reduced to $(5^{+4}_{-3})\times10^{-3}$ cts/(keV·kg·yr) by the PSD cut [2]. In Phase II the BI can be further reduced using a transparent nylon cylinder around the detector strings.

*Surface $\alpha$ contamination:* A second detector-intrinsic background is given by a potential $\alpha$-contamination of $^{226}$Ra daughter nuclides on the detector surface. Alpha-particles have a short range in germanium of the order of tens of µm, but are able to penetrate the 140 nm passivation layer in the detector groove and the 400 nm thick p+ electrode, respectively.

During the detector production at Canberra no special precautions were adopted such as handling under radon-free atmosphere. The four enriched BEGe detectors operated in the low background environment of the GERDA cryostat allowed to quantify the grade of the surface $\alpha$-contamination. In the data set used for GERDA Phase I data analysis [2] approximately 40 $\alpha$-like events with energies above 3 MeV were collected with the enriched BEGe detectors.

Figure 20 depicts the events from Fig. 10 in Ref. [4], which have energies above 3 MeV and were projected on the $A/E$ axis. Out of 43 candidates 39 were found with high $A/E$ values well beyond the threshold for $0\nu\beta\beta$-like SSE. These are mostly due to $\alpha$-events in agreement with the $A/E$ expectation from an $\alpha$-source irradiation of a p+ electrode of a BEGe detector inside a custom-made vacuum cryostat [25]. Out of these, 14 events with $A/E$>1 show strong pairwise time correlations. Since each pair or triple occurs in the same detector with a very similar $A/E$, it is suggestive that consecutive decays in $\alpha$ chains were observed which has caused some of the spikes in Fig. 20. A small fraction might also be due to $^{42}$K $\beta$-surface events. Moreover, one candidate populating the SSE band has a SSE like pulse shape, while three other events with $A/E$ <0.965 are identified in one case as a MSE and in two cases as surface background events with long rise times. Despite these few contaminating events from non-alpha sources, Fig. 20 clearly demonstrates that surface $\alpha$ events are efficiently rejected by the A/E cut.

## 5.2 Performance of BEGe detectors without passivation layer

As discussed in sections 4.3.3 and 5.1.2, the observed pulse shape degradation can be caused by charge carriers present or collected over time on the surface of the passivation layer between the anode and cathode of the diodes.

To examine if the effect is related to environmental conditions and can be improved for the operation in LAr, the detectors GD32A and GD35A were tested in the GERDA Detector Laboratory (GDL) [35] at LNGS. Both detectors were deployed in the same LAr test cryostat that has already been used for a long-term test

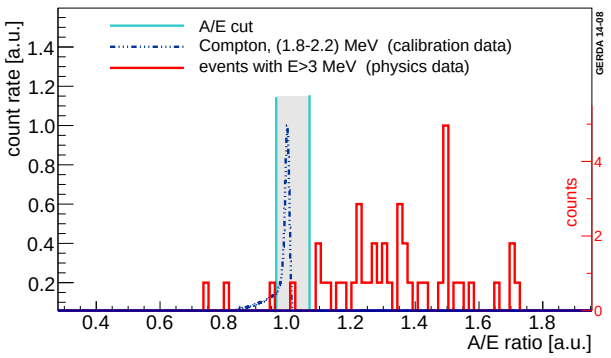


**Fig. 20** $A/E$ representation of the 43 events with energies above 3.0 MeV, which were registered with the four enriched BEGe detectors during GERDA Phase I. Events inside the gray area lie within the SSE band and are accepted by the PSD cut.

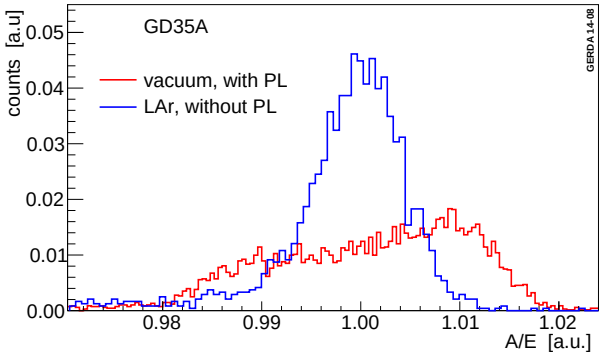


**Fig. 21** $A/E$ distributions of DEP events measured with detector GD35A under different conditions. Left: With passivation layer in vacuum. Right: Without passivation layer in LAr.

with a prototype depleted BEGe detector which was not passivated [45]. The two enriched BEGe detectors were operated in the standard configuration used in GERDA; i.e., bare detectors in LAr without passivation on the groove surface. According to Ref. [35,46] this is necessary in order to guarantee stable operation in LAr and a negligible increase of the leakage current.

The GDL LAr tests of the two detectors revealed a slightly increased energy resolution compared to the vacuum tests: in the case of detector GD32A it increased from 2.5 to 2.8 keV at 2615 keV, while in the case of GD35A it deteriorated from 2.4 to 3.0 keV. This was expected, since the distance of the first amplifying signal stage to the read-out electrodes was ∼60 cm in LAr and thus larger than in the vacuum setup.

The widths $b_{A/E}$ of the $A/E$ distributions of the two detectors GD32A and GD35A improved from 1.3 and 2.4% to 1.1 and 1.0%, respectively. The residual $A/E$ resolution was dominated by the noise of the GDL test set-up, and was similar to past measurements with prototype BEGe detectors. The strong non-Gaussian features observed in the HADES vacuum tests disappeared. As an example, both $A/E$ distributions for detector GD35A are depicted in Fig. 21. The $A/E$ distribution measured in GDL is consistent with a homogeneous pulse-shape response of the detector – a Gaussian SSE peak with a slight low $A/E$ tail due to bremsstrahlung.

The PSD survival efficiencies of $\gamma$-peaks and Compton-continua in $^{228}$Th source spectra were determined for detector GD32A: The SEP, FEP and Compton events at $Q_{\beta\beta}$ survive at 8.2, 11.5 and 38%, respectively. It should also be noted that for contaminants such as events from the detector n+ surface an improvement in $A/E$ resolution would have a greater effect on reducing the survival efficiency than for MSE dominated background contaminants such as $^{228}$Th.

## 6 Conclusions

This paper presents a detailed review of the production chain of the new GERDA Phase II broad energy germanium detectors. It discusses the performance of the first seven delivered detectors which were operated in vacuum and in liquid argon.

The detector production included an efficient isotopic enrichment of $^{76}$Ge from ∼8% in natural germanium to ∼88%, a successful purification and crystal growth. 30 crystal slices were obtained and converted into operational diodes. Only one diode did not fulfill all required performance specifications by showing charge collection deficiencies in the AV. In total, the 30 detectors have a mass of 20.0 kg which corresponds to a mass yield of 53%. The obtained impurity concentrations allowed for an operation of the detectors at relatively low voltages of (3-4) kV. During all production steps, the activation of the enriched germanium by cosmic radiation was kept at a minimum in order to meet the background specifications of GERDA Phase II. This was pursued by storing the germanium in underground sites near to the manufacturers and by using a shielded container for transportation. According to the tracked exposure histories and the predicted production rates of cosmogenic isotopes, the production of detectors underground – potentially needed in a future upgrade of the experiment for further background reduction [49] – was not necessary at this stage. Finally, more than 25% of the original germanium material was recovered for future crystal growth.

In order to characterize the detectors, an underground facility with the capability of screening two detectors per week was installed. For the tests the detectors were mounted in standard vacuum cryostats. As demonstrated by means of the first seven detectors, they all turned out to have excellent energy resolutions of 0.13% in terms of full widths at half maximum of the 1333 keV $^{60}$Co $\gamma$-line. This is an improvement of ∼30% compared to the GERDA detectors based on a semi-coaxial design. The active volume fraction was measured with a precision of a few percent. The pulse shape discrimination power was quantified. A previously unknown anomaly originating probably from surface charges deposited in the groove around the read-out electrode was identified. As a consequence, the PSD performance notably deteriorated for some detectors. Nonetheless, possibilities for improvement were found – either by chemical and thermal treatment of the passivation layer, or by removing the passivation entirely and handling the detector under clean nitrogen atmosphere.

Five out of the seven enriched BEGe detectors were deployed in the LAr cryostat of GERDA during Phase I of the experiment. It was the first time that this detector type was used in a $0\nu\beta\beta$ decay experiment. All but one were operated over almost 320 d. The leakage current and the energy scale were stable, while the energy resolution was ∼30% worse compared to their operation in vacuum. This was expected due to an increased distance of the first signal amplifying stages from the detectors. The pulse shape behavior experienced drifts in time which, however, could be corrected offline. A similar, but dynamic mechanism as observed in vacuum could be the reason for the effect. An appropriate modification of the passivation layer of the detectors is expected to keep leakage currents low and to cure the observed pulse shape degradations in LAr for GERDA Phase II.

Beta-decays of the $^{42}$Ar daughter nuclide $^{42}$K, and gamma-rays induced by $^{214}$Bi and $^{228}$Th decays were found to be the major contaminants affecting the background region at $Q_{\beta\beta}$ for the BEGe detectors in GERDA. The contribution from surface $\alpha$-events was of secondary order in the range of 5%. Moreover, the spectral fit of GERDA Phase I data confirmed agreement between the predicted and the fit-constrained contribution from cosmogenic isotope decays. Signals induced by most types of backgrounds can be efficiently removed by PSD cuts. Further background rejection will be possible by combining PSD with a veto by anti-coincidences between detectors or by scintillation light in LAr induced by contaminants. In addition, a transparent nylon cylinder around the detectors to stop mechanically the attracted $^{42}$K ions is in preparation. GERDA Phase II is expected to reduce its background by one order of magnitude compared to Phase I. The resulting background index of $10^{-3}$ cts/(keV·kg·yr) in the region of interest, the new additional detector mass and the improved energy resolution will allow for the exploration of half life values above $10^{26}$ yr for the $0\nu\beta\beta$ decay of $^{76}$Ge after a few years of data collection.

## Acknowledgments

The authors are grateful to JSC PA Electrochemical Plant in Zelenogorsk, PPM Pure Metals GmbH in Langelsheim, Canberra Industries Inc. in Oak Ridge, and Canberra Semiconductor N.V. in Olen for the prolific cooperation and enduring assistance.

The GERDA experiment is supported financially by the German Federal Ministry for Education and Research (BMBF), the German Research Foundation (DFG) via the Excellence Cluster Universe, the Italian Istituto Nazionale di Fisica Nucleare (INFN), the Max Planck Society (MPG), the Polish National Science Centre (NCN), the Foundation for Polish Science (MPD programme), the Russian Foundation for Basic Research, and the Swiss National Science Foundation (SNF). The institutions acknowledge also internal financial support.

The GERDA collaboration thanks the MAJORANA collaboration for sharing the underground site at Oak Ridge. Furthermore, we express our gratitude to the team of EIG EURIDICE on the premises of the Belgian Nuclear Research Center SCK•CEN, Mol. We thank the directors and the staff of the LNGS for their continuous strong support of the GERDA experiment.

## References

1. K.H. Ackermann et al., Eur. Phys. J. C **73** (2013) 2330
2. M. Agostini et al., Phys. Rev. Lett. **111** (2013) 122503
3. M. Agostini et al., Eur. Phys. J. C **74** (2014) 2764
4. M. Agostini et al., Eur. Phys. J. C **73** (2013) 2583
5. B. J. Mount, M. Redshaw, and E. G. Myers, Phys. Rev. C **81** (2010) 032501
6. H.V. Klapdor-Kleingrothaus et al., Eur. Phys. J. A **12** (2001) 147-154
7. C.E. Aalseth et al., Phys. Rev. D **65** (2002) 092007
8. D. Budjáš et al., J. Instrum. **4** (2009) P10007
9. M. Agostini et al., procs. of TIPP in print, TIPP 2014: Internat. Conference on Technology and Instrumentation in Particle Physics, 2-6 June 2014, Amsterdam
10. P. Vermaercke et al., Nucl. Instr. and Meth. A622 (2010) 433
11. J.R. De Laeter et al., Pure Appl. Chem. **75** (2003) 683
12. D. Budjáš et al., J. Instrum. **8** (2013) P104018
13. Joint Stock Company "Production Association Electrochemical Plant", Pervaya Promyshlennaya 1, 663690 Zelenogorsk, Russia; `http://www.ecp.ru/index_en.shtml`
14. A. N. Shubin et al., Atomic Energy **101** (2006) 588
15. Institute of Microelectronics Technology and High Purity Materials RAS, Academician Ossipyan Str 6, 142432 Chernogolovka, Russia; `http://www.ipmt-hpm.ac.ru/index.en.html`
16. State Scientific-Research and Design Institute of Rare-Metal Industry "Giredmet" JSC, B. Tolmachevsky lane 5-1, 119017 Moscow, Russia; `http://giredmet.ru/en/instituteen/`
17. PPM Pure Metals GmbH, Am Bahnhof 1, 38685 Langelsheim, Germany; `http://www.ppmpuremetals.de/`
18. Canberra Industries Inc., 107 Union Valley Rd, Oak Ridge, TN, USA; `http://www.canberra.com/`
19. E.E. Haller et al., Advances in Physics **30** (1981) 93
20. Canberra Semiconductor N.V., Lammerdries 25, 2250 Olen, Belgium ; `http://www.canberra.com/`
21. S. Hayakawa, Cosmic Ray Physics, John Wiley & Sons, Inc., NY (1969), ISBN-10: 0471363200, ISBN-13: 9780471363200
22. J.F. Ziegler, IBM J. Res. Dev. **40** (1996) 1
23. S. Cebrián et al., Astropart. Phys. **33** (2010) 316 *and references therein*
24. I. Barabanov et al., Nucl. Instrum. Meth. B **251** (2006) 115
25. M. Agostini, PhD thesis, Technische Universität München (2013) `http://www.mpi-hd.mpg.de/gerda/public/pub-phd.html`

26. P. Goldhagen et al., Nucl. Instrum. Meth. A **476** (2002) 42
27. A. Michel, diploma thesis, Technische Universität München (2012)
28. Z. He, Nucl. Instrum. Meth. A **463** (2001) 250
29. M. Agostini et al., J. Instrum. **6** (2011) P03005
30. E. Aguayo et al., Nucl. Instrum. Meth. A **701** (2013) 176
31. `http://www.canberra.com/products/detectors/cryostats-coolers.asp`
32. M. Agostini et al., J. Instrum. **6** (2011) P08013
33. M. Agostini et al., J. Phys.: Conf. Ser. **368** (2012) 012047
34. E. Andreotti et al., J. Instrum. **8** (2013) P06012
35. M. Barnabé-Heider, PhD thesis, University of Heidelberg (2009) `http://www.mpi-hd.mpg.de/gerda/public/pub-phd.html`
36. M. Agostini et al., J. Instrum. **6** (2011) P04005
37. N. Abgrall et al., Adv. High Energy Phys. **2014** (2014) 365432
38. D. Budjáš et al., Appl. Rad. Isot. **67** (2009) 706
39. M. Boswell et al., IEEE Trans. Nucl. Sci. 58 (2011) 1212
40. S. Agostinelli et al., Nucl. Instrum. Meth. A **506** (2003) 250
41. J. Allison et al., IEEE Trans. Nucl. Sci. **53** (2006) 270
42. G.A.P. Cirrone et al., Nucl. Instrum. Meth. A **618** (2010) 315
43. NIST Photon Cross Section Database: `http://www.nist.gov/pml/data/xcom/index.cfm`
44. I. Abt et al., Eur. Phys. J. C **68** (2010) 609
45. M. Barnabè-Heider et al., J. Instrum. **5** (2010) P10007
46. M. Barnabè-Heider et al., IEEE Conf. Nucl. Sci. Sym., October 2008, Dresden
47. NIST Stopping-Power and Range Tables for Electrons, Protons, and Helium Ions: `http://www.nist.gov/pml/data/star/`
48. A. Lazzaro, Master thesis, University Milano Bicocca (2012)
49. M. Hult et al., JRC Scien. Tech. Rep. (2008) EUR 23237 EN, ISBN: 978-92-79-08276-4